Electronic supplementary information (ESI) for

How does Excess Phenylalanine affect the Packing Density and Fluidity of a Lipid Membrane?

Shakkira Erimban, Snehasis Daschakraborty[*]

Department of Chemistry, Indian Institute of Technology Patna, Bihar 801106, India.

AUTHOR INFORMATION

Corresponding Author

[*]snehasis@iitp.ac.in

S1. Characteristic snapshots of different systems
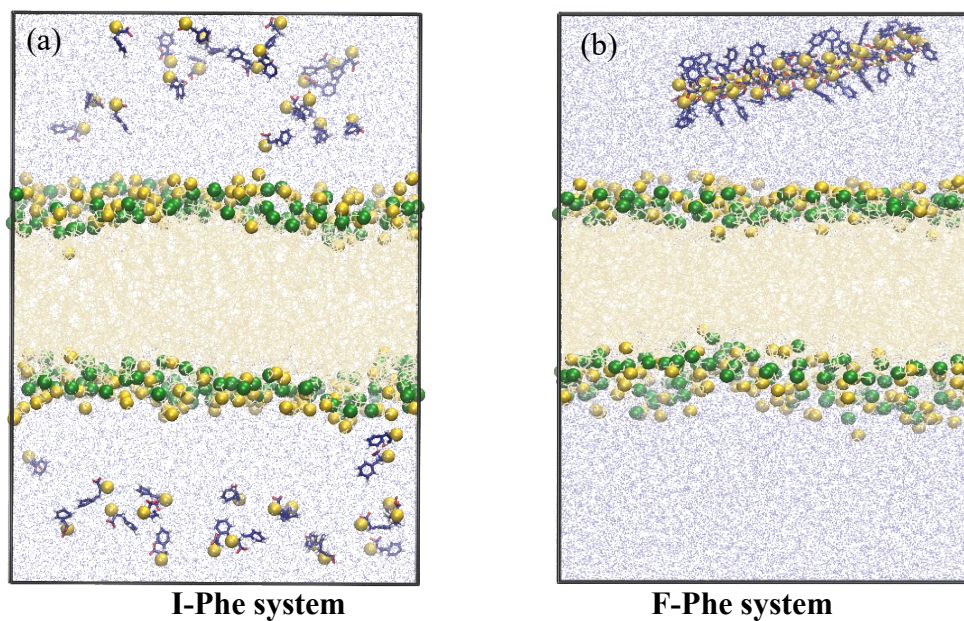

I-Phe system   **F-Phe system**

Figure S1. The initial configurations of (a) the larger I-Phe membrane system and (b) the larger F-Phe membrane system. Carbon atoms of Phe are color-coded with navy blue, nitrogen represented as spheres in yellow color, oxygen in red, and hydrogen in white. DPPC lipid molecules are colored in ochre and the phosphorous and nitrogen atoms are represented as VDW spheres in forest green and yellow color. Water molecules are colored with ice blue and represented as points.
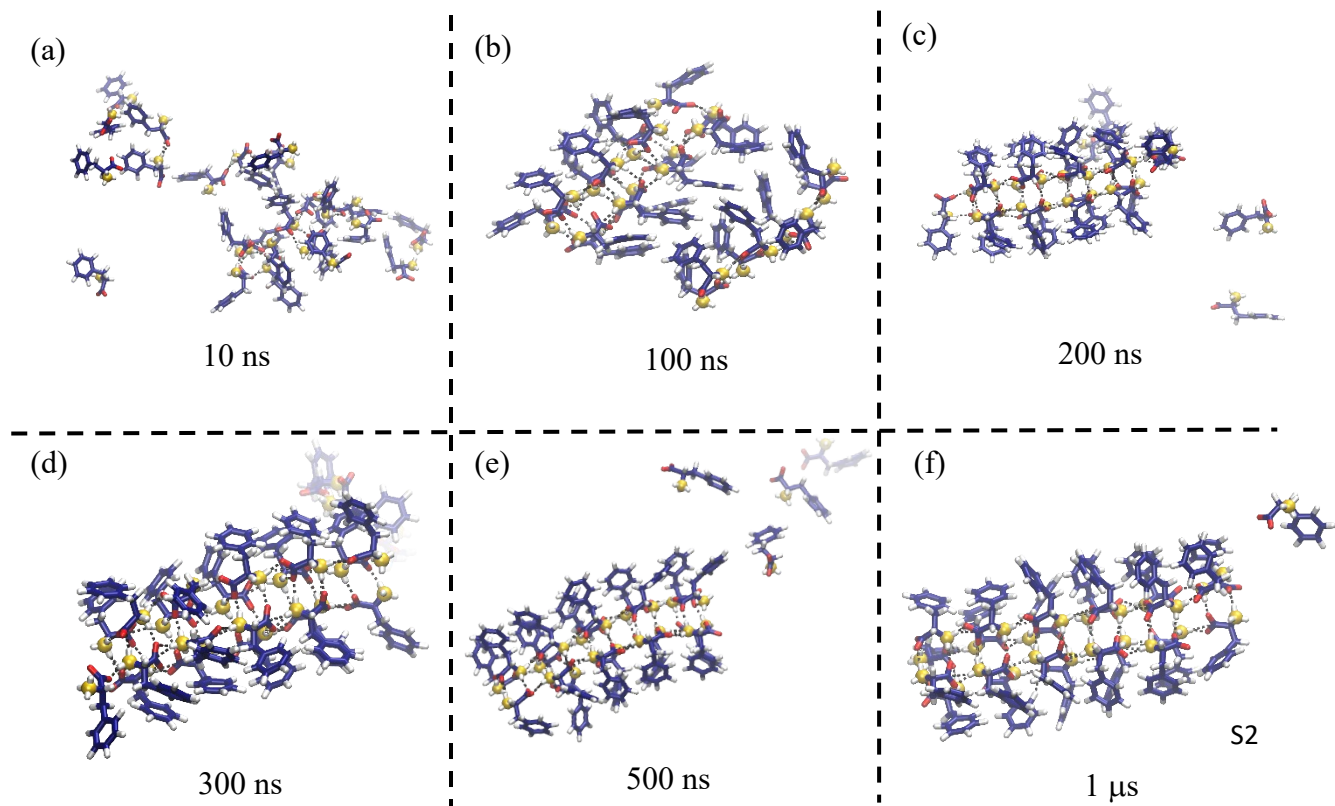

S2

Figure S2. The formation of the self-assembled structure 20-Phe from Phe monomer with time. Carbon atoms are color-coded with navy blue, nitrogen represented as spheres in yellow color, oxygen in red, and hydrogen with white.
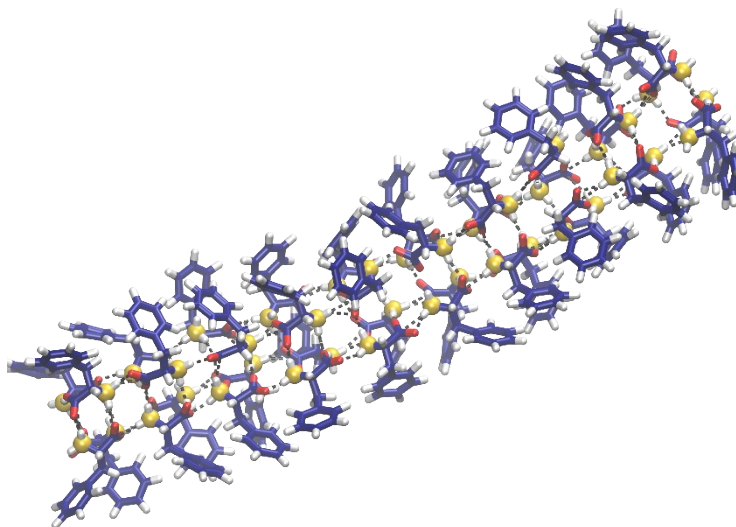

Figure S3. The equilibrium structure of 40-Phe at the end of 400 ns simulation. Carbon atoms are color-coded with navy blue, nitrogen represented as spheres in yellow color, oxygen in red, and hydrogen with white.

S2. Method of calculating the packing density parameters and water permeability

1. Calculation of Area per lipid $\langle A_L \rangle$

One of the simplest properties defining the structure of lipid bilayer, $<A_L>$ is defined by the average area occupied by each lipid molecule of the bilayer.[1-3] It is obtained by dividing the time-averaged lateral area of the simulation box by the number of lipid molecules present in each leaflet n_l.

$$\langle A_L \rangle = \langle A_{xy} \rangle / n_l \tag{1}$$

2. Calculation of Bilayer thickness $\langle T_L \rangle$

Another basic structural property defining the packing density of the bilayer is $<T_L>$. This is estimated from the time-averaged electron density profiles of the lipid bilayer. The peaks correspond to the phosphate atoms of the head group region. The peak-to-peak distance defines the total thickness of the bilayer.[2, 4] Figure S7 presents the electron density profiles for different systems.

3. Calculation of Isothermal area compressibility modulus K_A

This equilibrium defining property of the membrane defines the stress required to create anisotropic expansion in volume and is defined by [2, 3]

$$K_A = \frac{k_B T < A_L >}{n_L < \delta A_L^2 >}$$

(2)

where k_B is the Boltzmann constant, T is the simulation temperature, $<A_L>$ is the average area per lipid and δA_L^2 is the variance of A_L over the simulation, and n_l is the total number of lipids in the membrane system.

4. Calculation of Order parameter $\langle S_{CD} \rangle$

Another property defining the packing density of the bilayer is the order parameter. It defines the ordering of the hydrophobic interior of the lipid bilayer further defining the overall fluidity of the membrane.

$$S_{CD} = \frac{1}{2} < 3cos^2\theta - 1 >$$

(3)

Where θ defines the angle formed between a C-D bond of the methylene group of the hydrophobic tail and the bilayer normal. The order parameter values are calculated using the "gmx_order" analysis tool of Gromacs. The tool is used for the united atom model of lipids where we do not have the hydrogen/deuterium atoms. Thus, the tool creates the positions of these methylene-bound hydrogen/deuterium by locating the adjacent carbon atoms. This employs the tetrahedral geometry around the carbon atoms.[2, 5] However we have considered an all-atom model for DPPC lipid and thus we cross-checked the S_{CD} values from our program which are akin to gmx_order.

5. Evaluation of Water Permeability coefficient P

Membrane permeation is gauged from water permeability coefficient P. In an all-atom simulation, P can be calculated using various ways.[6-8] The transition rate-based counting method[6] (TB method) is one of the straightforward methods for estimating P.[9, 10] Principally, the method counts the number of crossing across the bilayer. Here permeability is defined by,

$$P = \frac{r}{2c_w}$$

(4)

$$r = \frac{Number\ of\ crossing}{A\ t_{traj}}$$

(5)

$$c_w = \frac{\bar{N}}{2V}$$

(6)

Where r is the transition rate across bilayer in either direction, c_w is the permeant concentration in water at equilibrium, A is the cross-sectional area of the bilayer, t_{traj} is the simulation time, $\overline{N}$ the average number of permeants, V defines the volume of the water compartment.

The number of successfully permeated water molecules is counted using the steps detailed elsewhere.[6] Fundamentally, the whole bilayer system is divided into five regions shown in Figure S4 for a Blank DPPC bilayer membrane. We track all the water molecules in region I with time. A successful permeation is counted only when one water molecule reaches the other side, region V through the regions II-III-IV. We have also counted the following crossings I-IV, I/II-IV, and I/II-V. However they over-predict the permeability and thus are not taken into account.
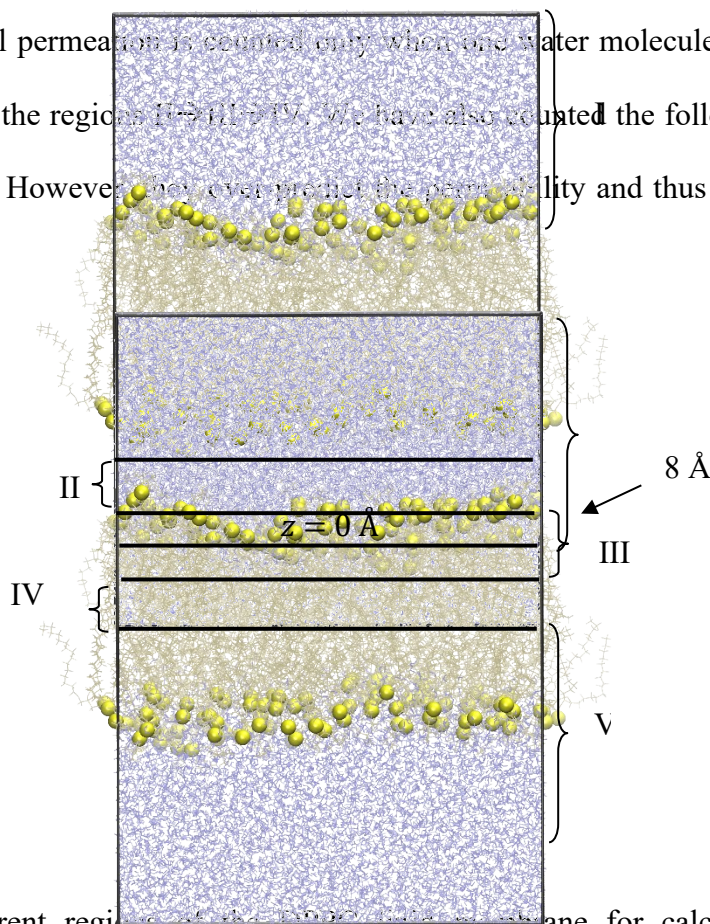

Figure S4. Five different regions of the DPPC lipid membrane for calculating the water permeability using the TB method. Water is represented as points color-coded with ice blue color, lipid molecules in ochre, and the phosphorous atoms of DPPC molecules with yellow color to mark the headgroup region of the bilayer.

S3. Results for the smaller membrane systems

Table S1. The effect of Phe on lipid membrane's structural properties, mechanical properties, and water permeability. The results for the larger membrane are presented in Table 1 of the main text.

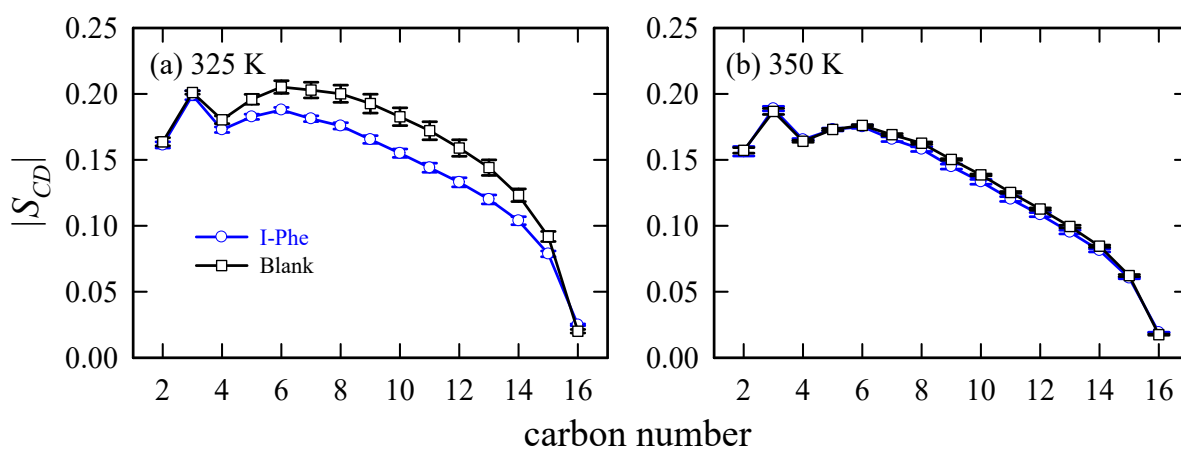| T(K)	System	$<A_L>$ (nm^2)	$<T_L>$ (nm)	K_A (N/m)	P ($\times 10^3$ cm^{-1})
325	I-Phe	0.72±0.00	3.12±0.02	0.19±0.03	8.48±1.66
	Blank	0.67±0.00	3.41±0.03	0.27±0.08	6.03±0.69
350	I-Phe	0.75±0.00	3.13±0.04	0.16±0.01	27.55±4.00
	Blank	0.71±0.00	3.32±0.05	0. 16±0.01	25.4±1.91

Figure S5. The deuterium order parameters of the carbon atoms (averaged over two acyl chains) for the smaller I-Phe and Blank membrane systems at 325 K (a) and 350 K (b).
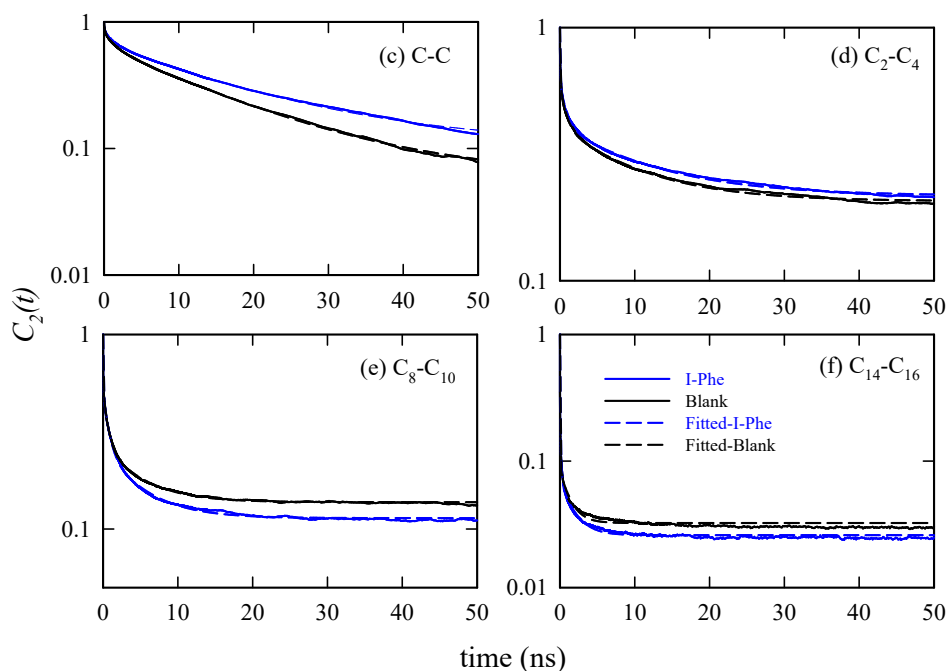
Figure S6. The reorientation correlation functions at 325 K for four characteristic regions of the lipid marked in the DPPC structure. The correlations (solid line) are fit to a function (dashed lines) with three exponentials and a constant:

$$C_2(t) = a_0 + \sum_{i=1}^{3} a_i e^{-t/\tau_i}$$

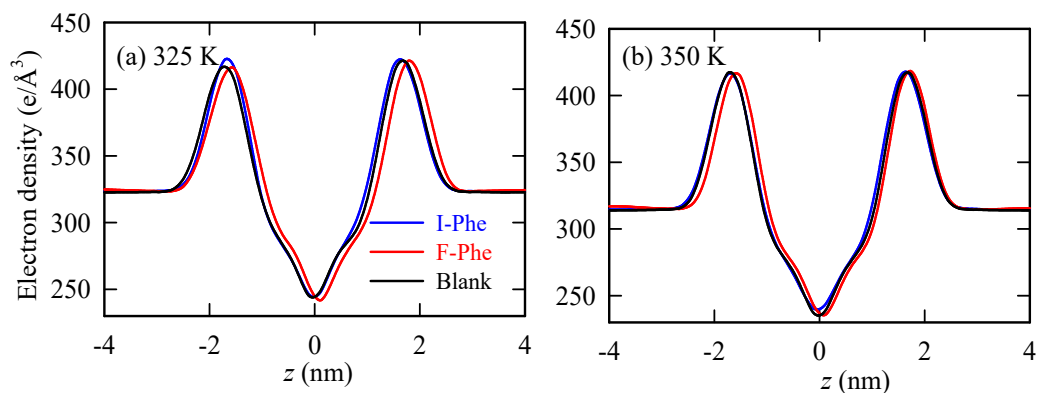## S4. Supporting results for the bigger membrane systems

Figure S7. Electron density profiles for I-Phe, F-Phe, and Blank systems at 325 K (a) and 350 K (b). The results are shown for the larger membrane systems.
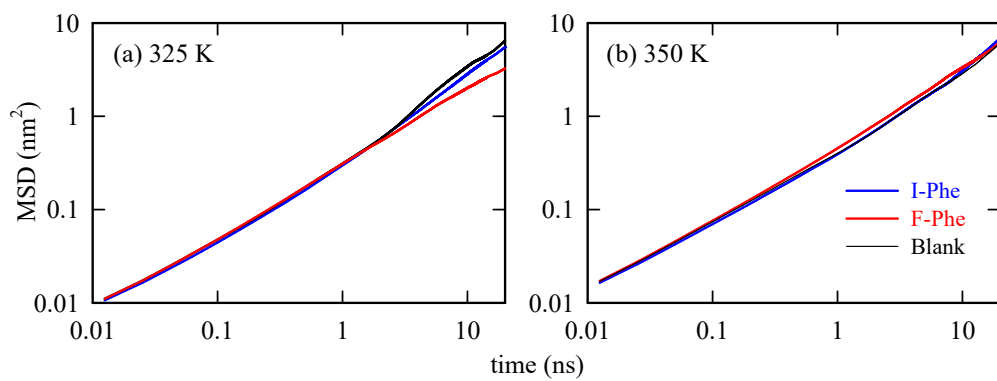
Figure S8. Lateral mean square displacements (MSD) of the lipid molecules at 325 K (a) and 350 K (b) for I-Phe, F-Phe, and Blank membrane systems. The results are shown here for the larger membrane systems.

Figure S9. Reorientation correlation functions, calculated for different vectors along the lipid for the larger membrane system at 325 K. All the correlations (solid line) are fit to a function

$$C_2(t) = a_0 + \sum_{i=1}^{3} a_i e^{-t/\tau_i}$$

(dashed lines) with three exponentials and a constant: . The Fitting parameters are presented in Table S2.

Figure S10. Reorientation correlation functions, calculated for different vectors along the lipid for the larger membrane system at 350 K. All the correlations (solid line) are fit to a function (dashed lines) with three exponentials and a constant:
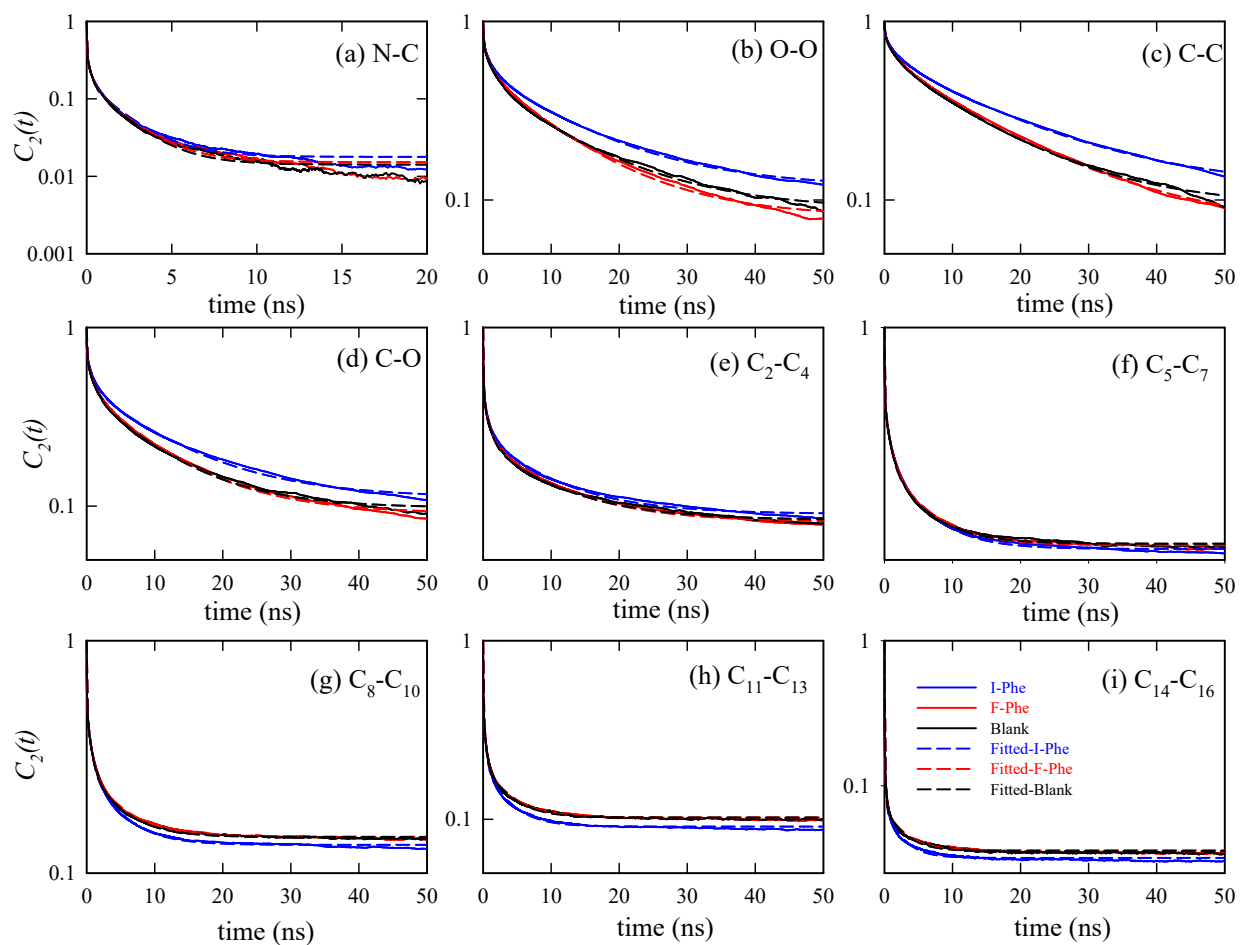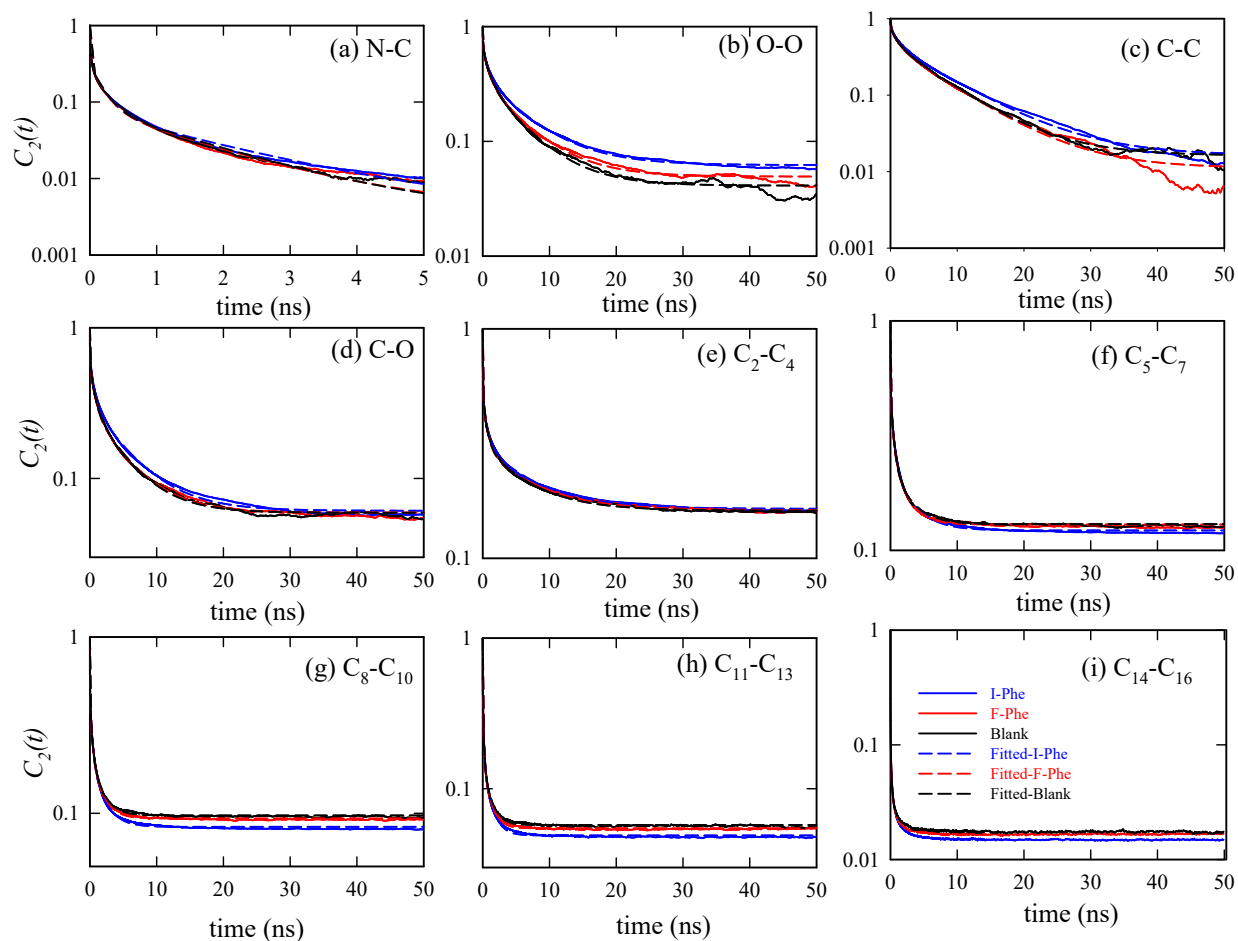
$$C_2(t) = a_0 + \sum_{i=1}^{3} a_i e^{-t/\tau_i}$$

The Fitting parameters are presented in Table S3.

Table S2. Fitting parameters of the correlation functions (Figure S9) at 325 K (larger membrane system). The correlations are fit to a function (dashed lines) with three exponentials and a constant:

$$C_2(t) = a_0 + \sum_{i=1}^{3} a_i e^{-t/\tau_i}$$

Region	System	a_1	a_2	a_3	a_0	$\tau_1(ns)$	$\tau_2(ns)$	$\tau_3(ns)$
N-C	I-Phe	0.61	0.22	0.14	0.02	0.01	0.24	2.00
	F-Phe	0.61	0.23	0.14	0.01	0.01	0.24	1.96
	Blank	0.60	0.23	0.15	0.01	0.01	0.22	1.92
O-O	I-Phe	0.25	0.23	0.40	0.12	0.06	1.33	14.29
	F-Phe	0.24	0.23	0.44	0.08	0.06	1.18	11.11
	Blank	0.27	0.27	0.37	0.09	0.07	1.67	12.50
C-C	I-Phe	0.17	0.20	0.52	0.11	0.09	1.89	16.67
	F-Phe	0.17	0.21	0.55	0.07	0.07	1.59	16.67
	Blank	0.17	0.20	0.53	0.09	0.08	1.61	14.29
C-O	I-Phe	0.30	0.24	0.35	0.11	0.03	1.08	12.50
	F-Phe	0.30	0.25	0.35	0.09	0.03	0.95	10.00
	Blank	0.31	0.26	0.33	010	0.03	1.03	10.00
C_2-C_4	I-Phe	0.38	0.20	0.20	0.22	0.04	0.76	10.00
	F-Phe	0.39	0.21	0.20	0.20	0.04	0.82	10.00
	Blank	0.40	0.21	0.18	0.21	0.04	0.93	10.00
C_5-C_7	I-Phe	0.43	0.21	0.19	0.16	0.03	0.74	5.26
	F-Phe	0.43	0.23	0.17	0.17	0.03	0.84	5.56
	Blank	0.43	0.23	0.17	0.17	0.03	0.81	5.26
C_8-C_{10}	I-Phe	0.46	0.24	0.16	0.13	0.02	0.61	4.35
	F-Phe	0.47	0.25	0.14	0.14	0.02	0.67	4.76
	Blank	0.47	0.24	0.15	0.14	0.02	0.61	4.35
C_{11}-C_{13}	I-Phe	0.52	0.28	0.11	0.09	0.02	0.33	3.23
	F-Phe	0.53	0.27	0.10	0.10	0.02	0.34	3.70
	Blank	0.52	0.27	0.10	0.10	0.02	0.34	3.45
C_{14}-C_{16}	I-Phe	0.77	0.16	0.04	0.03	0.01	0.14	2.27
	F-Phe	0.78	0.15	0.03	0.04	0.01	0.15	2.63
	Blank	0.78	0.15	0.04	0.04	0.01	0.15	2.50

Table S3. Fitting parameters of the correlation functions (Figure S10) at 350 K (bigger membrane system). The correlations are fit to a function (dashed lines) with three exponentials

$$C_2(t) = a_0 + \sum_{i=1}^{3} a_i e^{-t/\tau_i}$$

and a constant:

| Region	System	a_1	a_2	a_3	a_0	$\tau_1 (ns)$	$\tau_2 (ns)$	$\tau_3 (ns)$
N-C	I-Phe	0.70	0.22	0.07	0.004	0.01	0.21	1.85
	F-Phe	0.69	0.23	0.08	0.004	0.01	0.18	1.47
	Blank	0.69	0.23	0.08	0.003	0.01	0.18	1.54
O-O	I-Phe	0.33	0.31	0.30	0.06	0.05	0.90	6.25
	F-Phe	0.04	0.32	0.29	0.05	0.05	0.85	5.88
	Blank	0.35	0.31	0.30	0.04	0.05	0.93	5.56
C-C	I-Phe	0.24	0.29	0.44	0.02	0.07	1.27	8.33
	F-Phe	0.25	0.30	0.43	0.01	0.07	1.19	7.69
	Blank	0.24	0.29	0.45	0.02	0.06	1.06	7.14
C-O	I-Phe	0.38	0.30	0.26	0.06	0.02	0.68	5.56
	F-Phe	0.40	0.30	0.24	0.06	0.02	0.64	5.00
	Blank	0.39	0.30	0.25	0.06	0.02	0.61	4.76
C_2-C_4	I-Phe	0.47	0.21	0.15	0.16	0.03	0.66	2.94
	F-Phe	0.48	0.21	0.14	0.16	0.03	0.67	2.00
	Blank	0.47	0.22	0.15	0.16	0.03	0.60	2.63
C_5-C_7	I-Phe	0.51	0.26	0.12	0.12	0.02	0.51	2.94
	F-Phe	0.48	0.24	0.15	0.13	0.02	0.34	2.00
	Blank	0.50	0.26	0.11	0.13	0.02	0.47	2.63
C_8-C_{10}	I-Phe	0.52	0.26	0.13	0.08	0.01	0.30	1.72
	F-Phe	0.51	0.26	0.14	0.09	0.01	0.26	1.47
	Blank	0.51	0.26	0.13	0.10	0.01	0.26	1.49
C_{11}-C_{13}	I-Phe	0.55	0.29	0.10	0.05	0.01	0.14	1.11
	F-Phe	0.55	0.29	0.10	0.05	0.01	0.13	1.02
	Blank	0.56	0.29	0.09	0.06	0.01	0.13	1.06
C_{14}-C_{16}	I-Phe	0.66	0.27	0.05	0.01	0.00	0.03	0.49
	F-Phe	0.66	0.27	0.05	0.02	0.00	0.03	0.43
	Blank	0.66	0.27	0.05	0.02	0.00	0.03	0.45
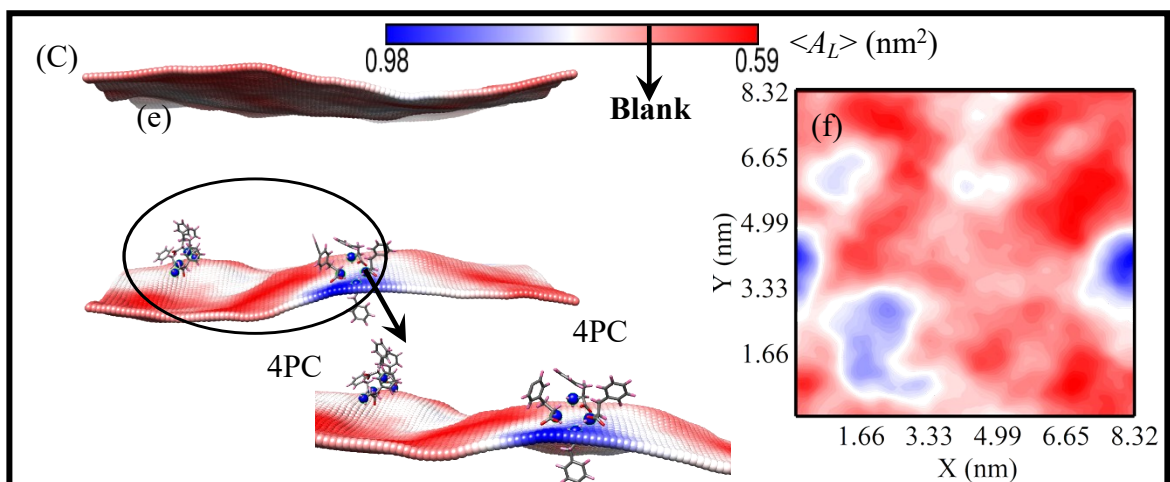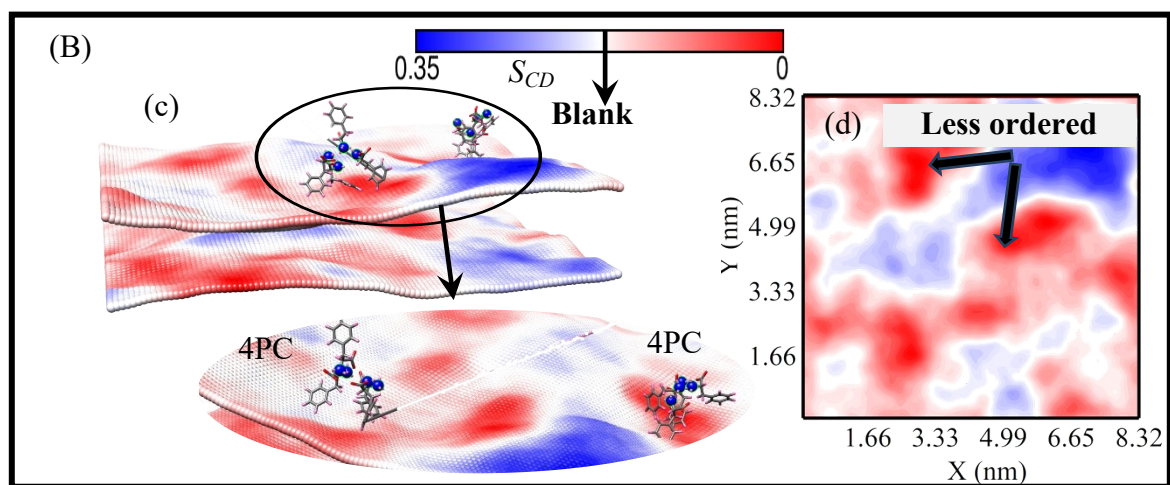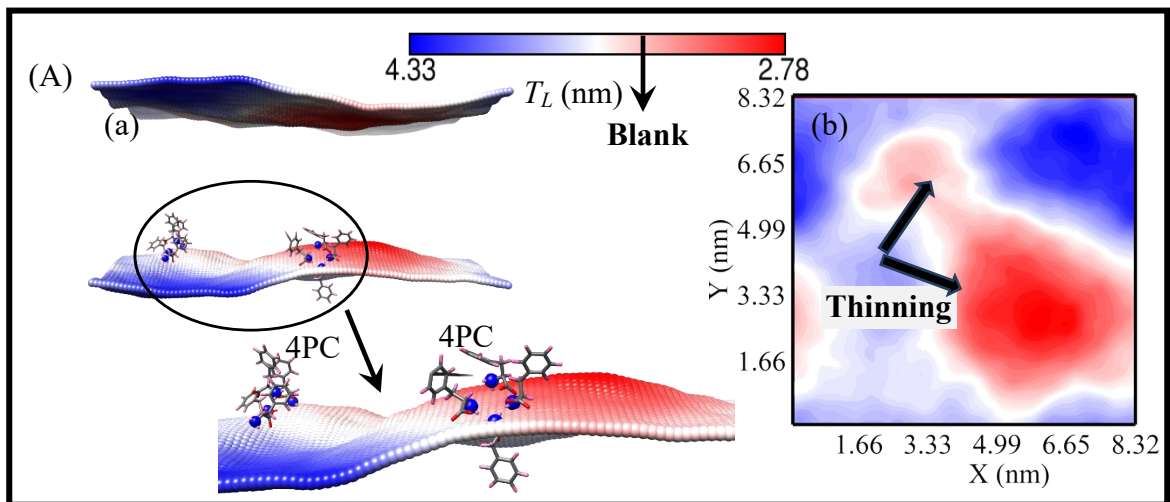
Figure S11. Two-dimensional profiles ((a), (c), (e)) and contour profiles ((b), (d), (f)) for the $<T_L>$ (A), $<S_{CD}>$ (B), and $<A_L>$ (C), calculated from the g_lomepro analysis tool[11] for the I-Phe system at 325 K for 20 ns from 540-560 ns . The average positions of two 4PCs, adsorbed on the bilayer surface, are also shown. The highlighted portions of the profiles in Figures (a) and (c) are shown enlarged. The average values of the three parameters for the Blank DPPC membrane are marked with an arrow on the respective color scale bars.
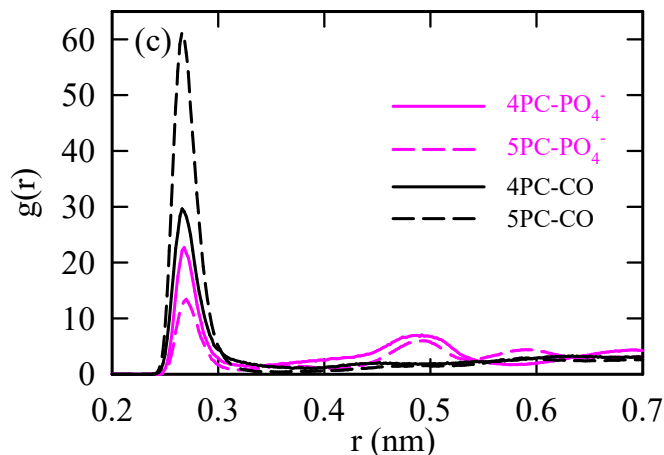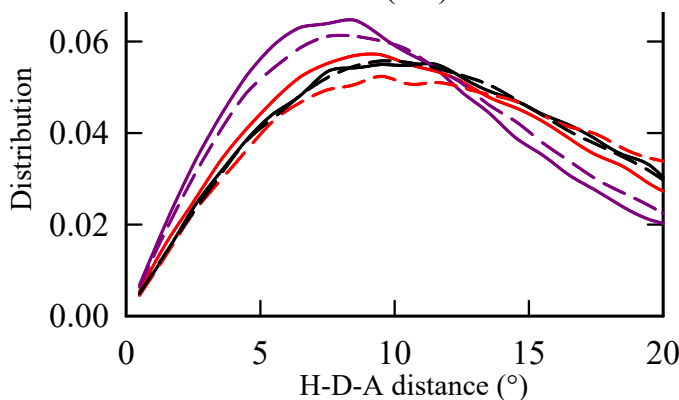

Figure S12. (a) and ... ons of all H-bonds formed by 4PC/5P ... and the number of intra-cluster H-bon ... n of 4PC and 5PC clusters around the ... 25 K. The profiles are averaged for th ...

S5. OPLS/AA I ...

Lipid mole ... or the first time, its parameterized by Maciejewski et al.[12, 13] for four characteristic lipids including DPPC. They provided a repository of all the parameters[14] including the mdp file to be used with Gromacs based simulation of membranes. The potential energy function for OPLS/AA FF is defined as,

$$V = \sum_i k_{b,i}(r_i - r_{o,i})^2 + \sum_i k_{\theta,i}(\theta_i - \theta_{o,i})^2 + \sum_i \left[\frac{1}{2}V_{1,i}(1 + \cos\varphi) + \frac{1}{2}V_{2,i}(1 - \cos 2\varphi) + \right.$$

$$\left. \frac{1}{2}V_{3,i}(1 + \cos 3\varphi) + \frac{1}{2}V_{4,i}(1 - \cos 4\varphi)\right] + \sum_i \sum_{j>i} \left\{\frac{q_i q_j e^2}{r_{ij}} + 4\varepsilon_{ij}\left[\left[\frac{\sigma_{ij}}{r_{ij}}\right]^{12} - \left[\frac{\sigma_{ij}}{r_{ij}}\right]^6\right]\right\} \quad (7)$$

Where it is a sum of different energies including harmonic bond stretching, angle bending, torsional energy, Coulomb, and 12-6 Lennard Jones energy respectively.
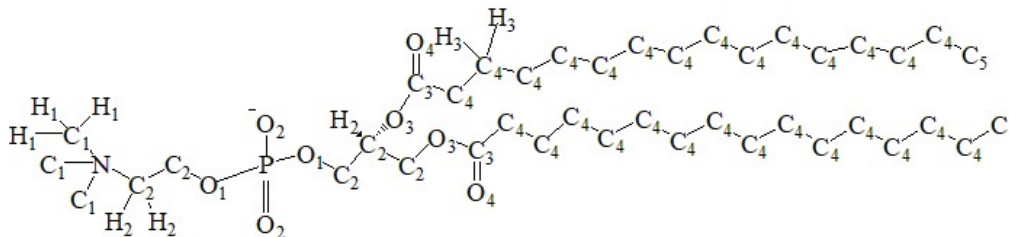

Figure S13. Nomenclature of 14 different atom types in our DPPC lipid molecule modeled by OPLS/AA FF.

Table S4. OPLS/AA FF parameters including charge, sigma, and epsilon values for calculating the non-bonded interaction energy for different atom types in DPPC lipid molecule.

Atoms	q (e)	σ (nm)	ε (kJmol^{-1})
C_1	-0.2795	0.35	0.276144
C_2	-0.1311	0.35	0.276144
C_3	0.9766	0.375	0.43932
C_4	-0.1200	0.3376	0.276144
C_5	-0.1800	0.3376	0.276144
H_1	0.1484	0.25	0.12552
H_2	0.1484	0.25	0.12552
H_3	0.0600	0.2468	0.12552
O_1	-0.6096	0.29	0.58576
O_2	-0.9666	0.315	0.8368
O_3	-0.5083	0.3	0.71128
O_4	-0.6887	0.296	0.87864
N	0.3372	0.325	0.71128
P	1.5572	0.374	0.8368

Table S5. OPLS/AA FF parameters for harmonic bond stretching energy calculation for different bond types in DPPC lipid molecule.

Bonds	r_o (nm)	k_b (kJmol^{-1}nm^{-2})
C_1-H_1	0.109	284512
C_1-N	0.1471	307105.6
N-C_2	0.1471	307105.6
C_2-H_2	0.109	284512
C_2-C_2	0.1529	224262.4
C_2-O_1	0.141	267776
P-O_1	0.148	439320
P-O_2	0.161	192464
C_2-O_3	0.141	267776
C_3-O_3	0.1327	179075.2
C_3-O_4	0.1229	476976
C_3-C_4	0.1522	265265.6
C_4-C_4	0.1529	224262.4
C_4-C_5	0.1529	224262.4
C_4-H_4	0.109	284512
C_5-H_4	0.109	284512

Table S6. OPLS/AA FF parameters for harmonic angle bending energy calculation for different angle types in DPPC lipid molecule.

Angles	θ_o (nm)	K_θ (kJmol^{-1}rad^{-2})
H_1-C_1-H_1	107.8	276.144
N-C_1-H_1	109.5	292.88
C_1-N-C_1	109.5	292.88
N-C_2-H_2	109.5	292.88
H_2-C_2-H_2	107.8	276.144
C_2-C_2-H_2	110.7	313.8
N-C_2-C_2	111.2	6.6944
C_2-C_2-O_1	109.5	418.4
C_2-O_1-P	120.5	836.8
O_2-P -O_1	108.23	836.8
O_2-P -O_2	119.9	117.152
C_2-C_2-C_2	112.7	488.2728
C_2-C_2-O_3	109.5	418.4
C_2-O_2-C_3	116.9	694.544
O_3-C_3-O_4	123.4	694.544
O_4-C_3-C_4	120.4	669.44
C_3-C_4-C_4	111.1	5.27184
C_4-C_4-H_3	110.7	313.8
H_3-C_4-H_3	107.8	276.144
C_4-C_4-C_4	112.7	488.2728
C_5-C_4-C_4	112.7	488.2728
C_4-C_5-H_3	110.7	313.8

The OPLS/AA parameters are converted to Ryckaert-Bellemans parameters as follows:

$$C_0 = V_2 + \frac{1}{2}(V_1 + V_3) \qquad (8)$$

$$C_1 = \frac{1}{2}(-V_1 + 3V_3) \qquad (9)$$

$$C_2 = (-V_2 + 4V_4) \qquad (10)$$

$$C_3 = (-2V_3) \qquad (11)$$

$$C_4 = (-4V_4) \qquad (12)$$

$$C_5 = 0 \qquad (13)$$

Table S7. OPLS/AA FF parameters for Ryckaert-Bellemans (RB) dihedral potential calculation for different dihedral angle types in DPPC lipid molecule.

Dihedrals	C_0 (kJmol^{-1})	C_1 (kJmol^{-1})	C_2 (kJmol^{-1})	C_3 (kJmol^{-1})	C_4 (kJmol^{-1})	C_5 (kJmol^{-1})
H_1-C_1-N-C_1	0.63116	1.89347	0.00000	-2.52463	0.00000	0.00000
C_1-N-C_2-H_2	0.63116	1.89347	0.00000	-2.52463	0.00000	0.00000
O_1-C_2-C_2-H_2	0.97906	2.93717	0.00000	-3.91622	0.00000	0.00000
C_2-O_1-P-O_2	0.00000	0.00000	0.00000	0.00000	0.00000	0.00000
C_2-C_2-C_2-H_2	0.62760	1.88280	0.00000	-2.51040	0.00000	0.00000
H_2-C_2-C_2-H_2	0.62760	1.88280	0.00000	-2.51040	0.00000	0.00000
O_3-C_2-C_2-O_3	1.66966	-10.5566	6.80534	-1.61	-1.91353	6.19098
C_3-O_3-C_2-H_2	0.41422	1.24265	0.00000	-1.65686	0.00000	0.00000
C_2-O_3-C_3-O_4	21.43882	0.00000	-21.43882	0.00000	0.00000	0.00000
O_4-C_3-C_4-C_4	0.00000	0.00000	0.00000	0.00000	0.00000	0.00000
O_4-C_3-C_4-H_3	0.00000	0.00000	0.00000	0.00000	0.00000	0.00000
O_3-C_3-C_4-H_3	0.27614	0.82843	0.00000	-1.10458	0.00000	0.00000
H_3-C_4-C_4-C_4	0.62760	1.88280	0.00000	-2.51040	0.00000	0.00000
H_3-C_4-C_4-H_3	0.62760	1.88280	0.00000	-2.51040	0.00000	0.00000
C_4-C_4-C_4-C_4	1.81211	-0.948788	-3.15209	1.32173	4.32914	-3.39430
C_4-C_4-C_5-H_3	0.62760	1.88280	0.00000	-2.51040	0.00000	0.00000
C_5-C_4-C_4-C_4	1.81211	-0.948788	-3.15209	1.32173	4.32914	-3.39430

S6. Comparison of the Simulated DPPC Lipid Membrane Properties using the OPLS/AA force-field (FF) with Literature Experiment and Simulation Studies using CHARMM36, GROMOS96, and LIPID14 FFs.

For the simulations of DPPC lipid membrane, the CHARMM and AMBER FFs are more frequently used compared to the OPLS/AA FF for lipid, which is relatively new. The OPLS/AA FF for lipid membrane was first parameterized by Maciejewski et al.[12-14] The simulated structural and dynamical properties of the lipid membrane are in good agreement with the experimental data. We have also made a detailed comparison of different simulated properties of DPPC lipid membrane at 325 K with the literature simulations using three others FFs (CHARMM36, GROMOS96, LIPID14). Table S8 presents a comparison of the area per lipid $<A_L>$, average

thickness $<T_L>$, isothermal compressibility K_A, lateral diffusion of lipid D_{xy}, water permeability P, and fluid-gel phase transition temperature T_m. The deuterium order parameters for the acyl chains of the lipids, modeled by different FFs are presented in Figure S14. Summarily, the membrane packing parameters, lipid diffusion, water permeability, and the fluid/gel phase transition temperature of the DPPC lipid membrane from the simulation with OPLS/AA FF agree with both experimental and prior simulation data using different FFs.

Table S8. Validating different structural, dynamic, mechanical, and functional properties of DPPC lipid from OPLS/AA FF with Expt. and other FF. The structural property for CHARMM36 is calculated from this study.

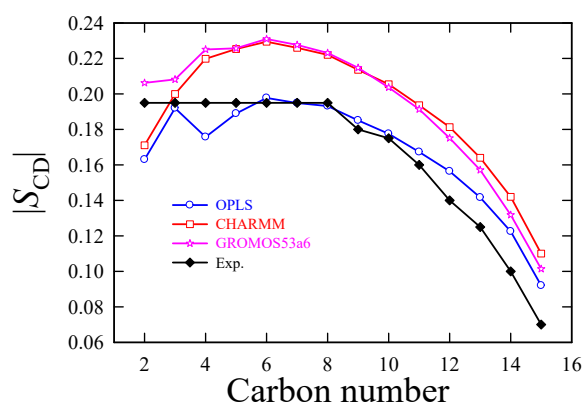| T(K)	System	$<A_L>$ (nm^2)	$<T_L>$ (nm)	K_A (N/m)	$D_{xy}/10^{-8}$ (cm^2/s)	P (×10^3 cm^{-1})	T_m (K)
	OPLS/AA	0.66	3.44	0.16	10.8	4.75	336
	CHARMM36	0.61	3.86	0.19	17	4.85	353[15]
325	GROMOS53a6	0.6[4]	3.59[4]	0.48[4]	17.21[4]	–	338[15]
	GROMOS54a7	0.65[16]	3.51[16]	–	4.1[16]	–	335[17]
	LIPID14	0.62[18]	3.79[18]	0.244[18]	9.21[18]	–	343[17]
	Exp.	0.57-0.72[19, 20]	3.42-3.83[21, 22]	0.231[21]	14[23]		314[24]

Figure S14. Deuterium order parameter averaged for the two acyl chains of DPPC bilayer predicted from OPLS/AA FF is compared with CHARMM36, GROMOS53a6[4], and experiment.[25]

The fluid-gel phase transition temperature (T_m) for OPLS/AA FF is calculated from annealing simulations. First, the DPPC lipid membrane is allowed to slowly cool from 350 to 280 K at a rate of 1 K/ns. A similar cooling rate was also used in prior simulation studies[15, 17, 26, 27]. Next, we perform a long simulation to ensure the formation of the gel phase of the membrane. Starting from the resulting gel phase we heat the system again to 350 K with a heating rate of 1 K/ns. The area per lipid A_L is followed by temperature in Figure S15. The gel to the fluid phase transition is captured by the sharp transition of A_L around $T_m \sim 336$ K, the midpoint of the sharp transition region.
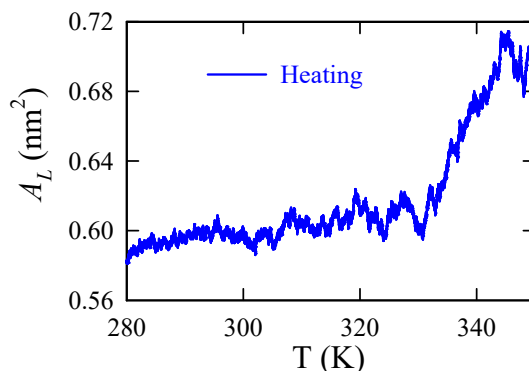
Figure S15. The area per lipid A_L as a function of temperature during heating of the DPPC lipid membrane modeled by OPLS/AA FF.

S7. Analysis of the Simulation with CHARMM36 FF

Apart from the fact that the OPLS/AA model of lipid can predict the structural and dynamical properties of lipid membrane with good accuracy, there is another more important reason for choosing the OPLS/AA FF for lipids in the present study. As seen in previous simulation studies, the OPLS/AA FF for Phe successfully captures the formation of fibrillar self-assembly of Phe in bulk water. As seen in the present work and prior simulation studies, the self-assembly of Phe in bulk water is well explored using the OPLS/AA FF of Phe. On the other

hand, a previous simulation study[28] already commented on the failure of CHARMM27 FF in predicting the self-aggregation behavior of Phe monomers in an aqueous solution.

We now attempt to check the applicability of CHARMM36 FF of Phe in the present study. First, we check the self-assembly of Phe in an aqueous solution. Next, we study the interaction of Phe with the DPPC lipid membrane. The CHARMM36 FF of DPPC lipid is considered here. The FF parameters for the lipid and Phe are generated using the online tool CHARMM-GUI membrane builder.[29] Water is modeled using mTIP3P FF (also known as CHARMM TIP3P model or mTIP3P).

1. Phe in Aqueous Solution

Spontaneous formation of fibril-like aggregates of Phe in aqueous solution was confirmed in different experimental and simulation studies. In the pioneering work by Adler-Abramovich et al.[30], the authors showed that Phe self-assembles into fibrils with amyloid-like morphology. A mass spectrometry-based study confirmed the formation of fibrillar Phe aggregation with a four-fold symmetry at neutral pH, which is composed of multiple layers of four zwitterionic monomers.[31] The zwitterionic termini of Phe form the hydrophilic interior of the self-assembly, while the exterior is hydrophobic since the aromatic phenyl group is exposed outside. Later on, similar self-assembled structures are captured from OPLS/AA FF-based simulations.[32, 33] Therefore, the applicability of any FF in this work lies in the potential of self-assembly of Phe in an aqueous solution.

We start simulating the aqueous solution of CHARMM36 Phe from two different initial configurations. In one setup (setup-I), we start from the configuration where Phe monomers are randomly packed with water. In the other setup (setup-II), we introduce the self-assembled

structure of 20 Phe monomer obtained from the OPLS/AA simulation to an equilibrated water box. In (I), we pack 24 Phe monomers randomly in 3700 water molecules, similar to that in OPLS/AA simulation. We simulate the system using the NPT ensemble for 1 μs time NPT simulations at 350 K and 325 K temperature and 1 bar pressure. Temperature and pressure are coupled using Berendsen thermostat and Parrinello-Rahman barostat.[34] Relaxation time constant of 0.5 and 1.0 ps are used for the thermostat and barostat respectively. Bond lengths involving hydrogens were constrained with LINCS algorithm.[35]

Unlike in OPLS/AA simulation, we do not observe any self-aggregation of Phe monomers forming a fibril-like structure. Figure S16 shows snapshots showing the evolution of the system over 1 μs simulations for 350 K. The cluster size distribution averaged over the last 600 ns is shown in Figure S17. The self-assembled structure of Phe has not formed at the end of the 1 μs simulation. The probability of having monomers is still more. The picture remains the same at 325 K. In the second system (setup-II) with the self-assembled structure of Phe, we perform 1 μs NPT simulation under similar simulation conditions of setup-I. We observe a gradual breakdown of the fibril structure into separate monomers. The cluster size distributions at different time intervals are shown in Figure S18. Figure S19 shows the progressive breaking pathway of Phe fibril during the 1 μs simulation run.
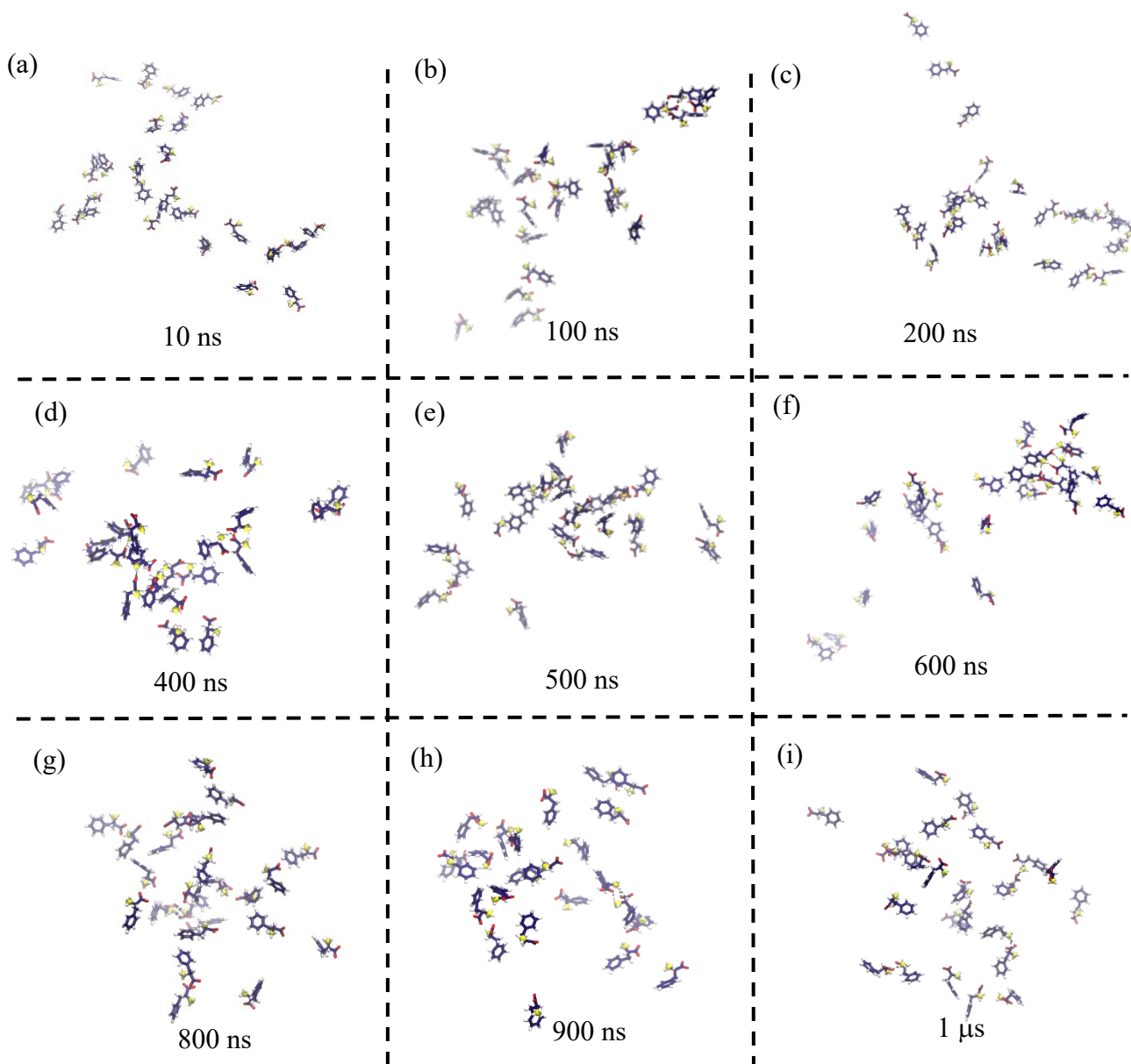
Figure S16. Snapshots of the aqueous solution of Phe (setup-I) at 350 K at different times during 1 μs simulation trajectory. Phe is modeled with CHARMM36 FF.

These show the failure of CHARMM36 FF of Phe for the formation of a self-assembled structure of Phe in an aqueous solution. This is consistent with the previous observation[28] for CHARMM27 FF of Phe. We compare the intermolecular FF parameters, atomic charge, sigma, and epsilon values for all the 23 atoms of the Phe molecule in Table S9. The key differences

between the CHARMM36 and OPLS/AA FFs exist in the atomic charges and Lennard-Jones (LJ) parameters of the carboxylate oxygen (O). The higher negative charge of O and larger LJ well depth of O result in stronger H-bonding between Phe monomers, which induces further aggregation to form the self-assembled structure of Phe.
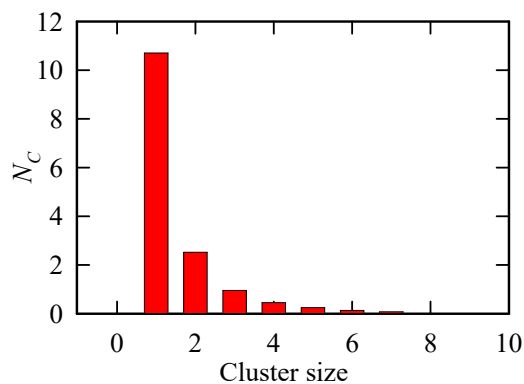
Figure S17. Cluster size distribution of CHARMM36 Phe in water at 350 K (setup-I). The analysis is performed for the last 600 ns of the 1 µs simulation trajectory.
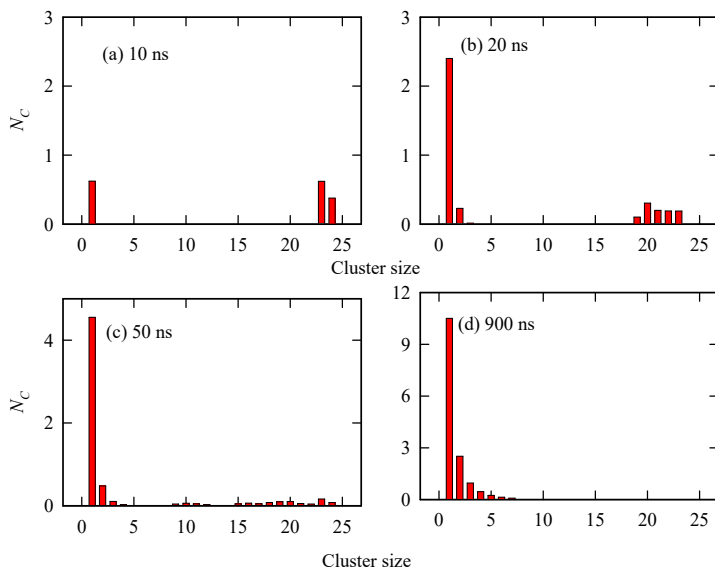

Figure S18: Cluster size distribution of CHARMM36 Phe in water (setup-II) at 350 K for different time during the 1 µs simulation trajectory.
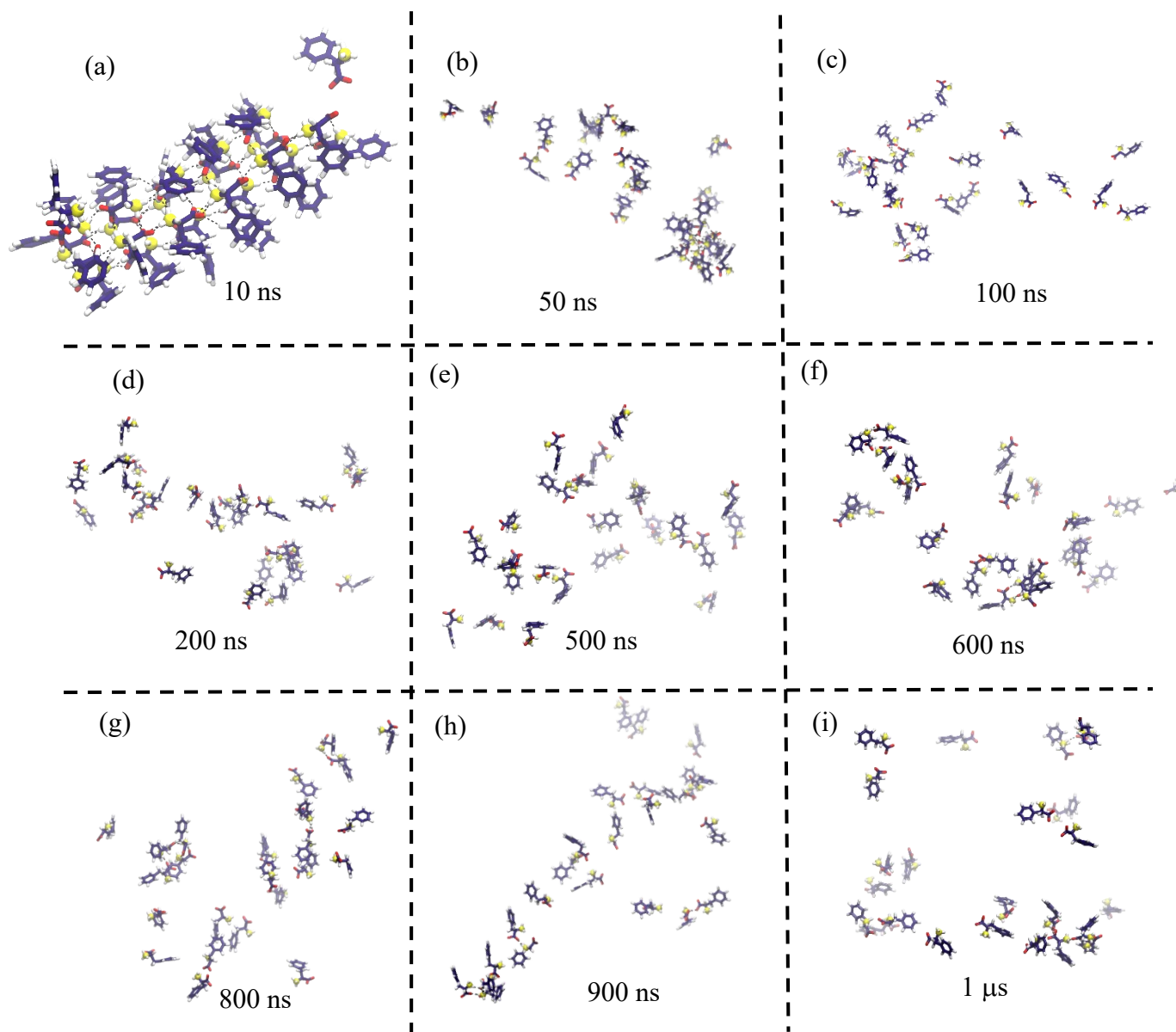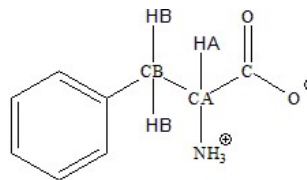
Figure S19. Snapshots showing the gradual dissolution of the self-assembled fibrillar structure of Phe, modeled with CHARMM36 FF in aqueous solution (setup-II).

Table S9. Parameter set for some of the atoms of Phe molecule in OPLS/AA, CHARMM36, and CHARMM27 FF. The atom notations in the first column are labeled in the structure given below.

Atom	$q(e)$			$\sigma/10^{-1}$ (nm)			$\varepsilon/10^{-1}$ (kJmol^{-1})		
	OPLS/ AA	CHAR MM36	CHAR MM27	OPLS/ AA	CHAR MM36	CHAR MM27	OPLS/ AA	CHAR MM36	CHAR MM27
N	-0.300	-0.30	-0.300	3.250	3.296	3.296	7.113	8.368	8.368
H	0.330	0.330	0.330	0.000	0.400	0.400	0.000	1.925	1.925
C	0.700	0.340	0.340	2.960	3.564	3.564	4.393	2.929	2.929
O	-0.800	-0.670	-0.670	2.960	3.029	3.029	8.786	5.021	5.021
CA	0.150	0.210	0.210	3.500	3.564	4.035	2.761	1.339	0.837
HA	0.060	0.100	0.100	2.500	2.352	2.352	1.255	9.205	9.205
CB	-0.005	-0.18	-0.180	3.500	3.581	3.875	2.761	2.343	2.301
HB	0.060	0.10	0.100	2.500	2.388	2.352	1.255	1.423	0.920

Phe

2. Interaction of Phe with lipid membrane

We also check the applicability of CHARMM36 FF in probing the interaction of Phe molecules with the DPPC lipid membrane. The simulation setup for the CHARMM36 simulation is the same as the OPLS/AA FF simulation. However, since the fibrillar structure did not form in the aqueous solution of Phe, we do not consider the F-Phe system. The I-Phe system is simulated at 310, 325, and 350 K. The Blank membrane systems are also simulated at the same temperatures. The CHARMM36 simulation protocol is the same as the OPLS/AA simulation, as described in Sec. S1. The lipid membrane undergoes the fluid-gel phase transition at 310 K. This is expected since the fluid-gel phase transition temperature (T_m) of the DPPC membrane, modeled with CHARMM36 FF, is ~350 K, which is much higher than 310 K. Therefore, we analyze only for two temperatures 325 K and 350 K.

Unlike the OPLS/AA simulation, Phe does not intercalate strongly in the membrane at any temperatures. The time-dependent evolution of the system is shown in Figure S20 and S21 at 325 and 350 K, respectively. The majority of the Phe monomers remain dispersed in the water region

outside the DPPC lipid membrane. The snapshots also suggest that the Phe monomers do not aggregate also to form fibrillar structures. For a quantitative estimation of the cluster size, we analyze the numbers of Phe monomer (1-Phe), Phe-dimer (2PC), and Phe-trimer (3PC) at different time intervals, averaging over 50 ns time during 700 ns simulation trajectory. These are shown in Figure S22. Therefore, the CHARMM36 simulation fails to mimic the interaction between Phe and DPPC lipid membrane, as seen in experiments.[30, 36-38]

Figure S20. Snapshots of the I-Phe system showing the time-dependent structure of Phe near the DPPC lipid membrane modeled with CHARMM36 FF at 325 K. The DPPC head group atoms are shown in green VDW beads, while the acyl chains are color-coded with gray. The Phe molecules are color-coded as follows: blue (carbon), purple (nitrogen), and red (oxygen).
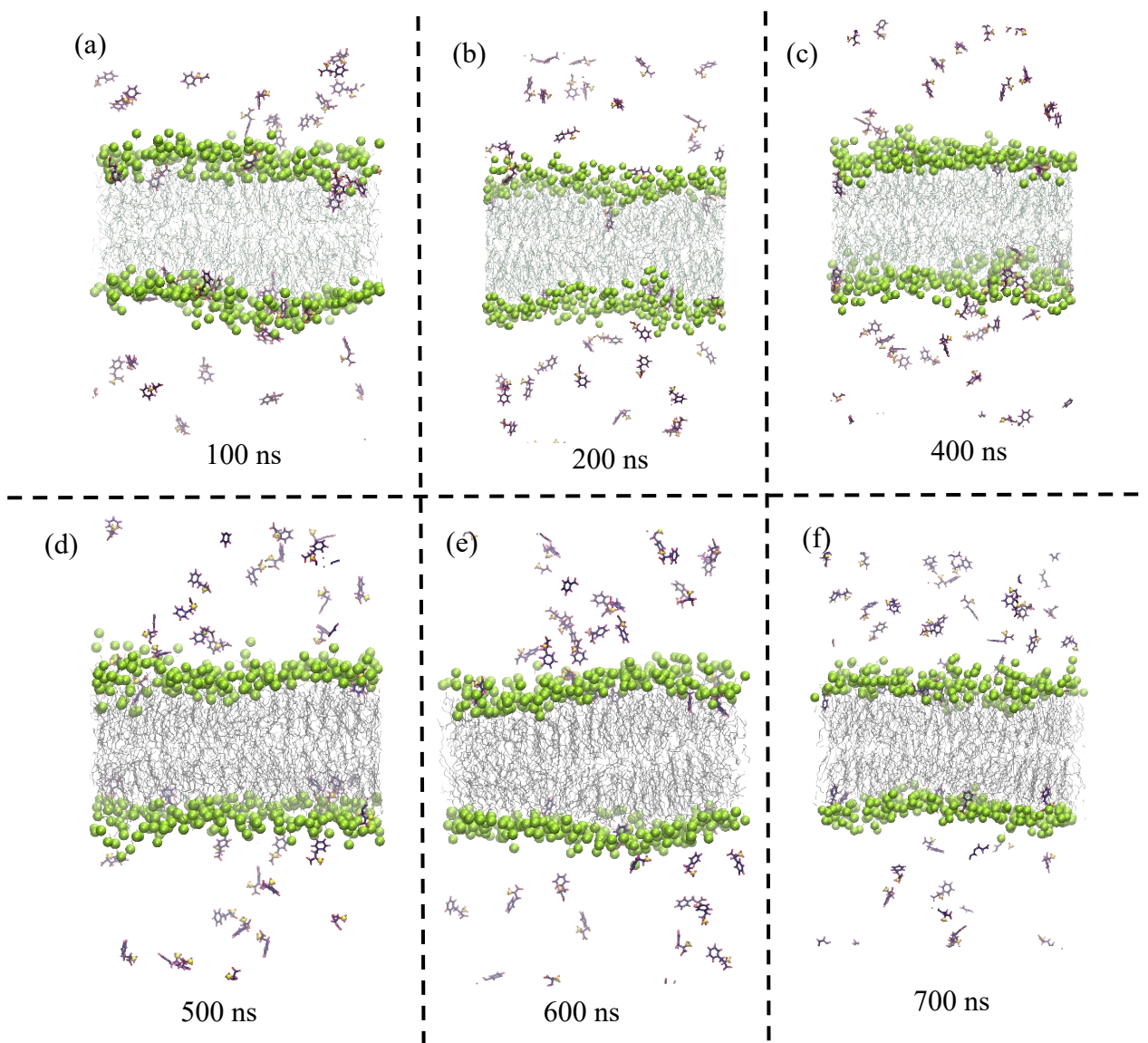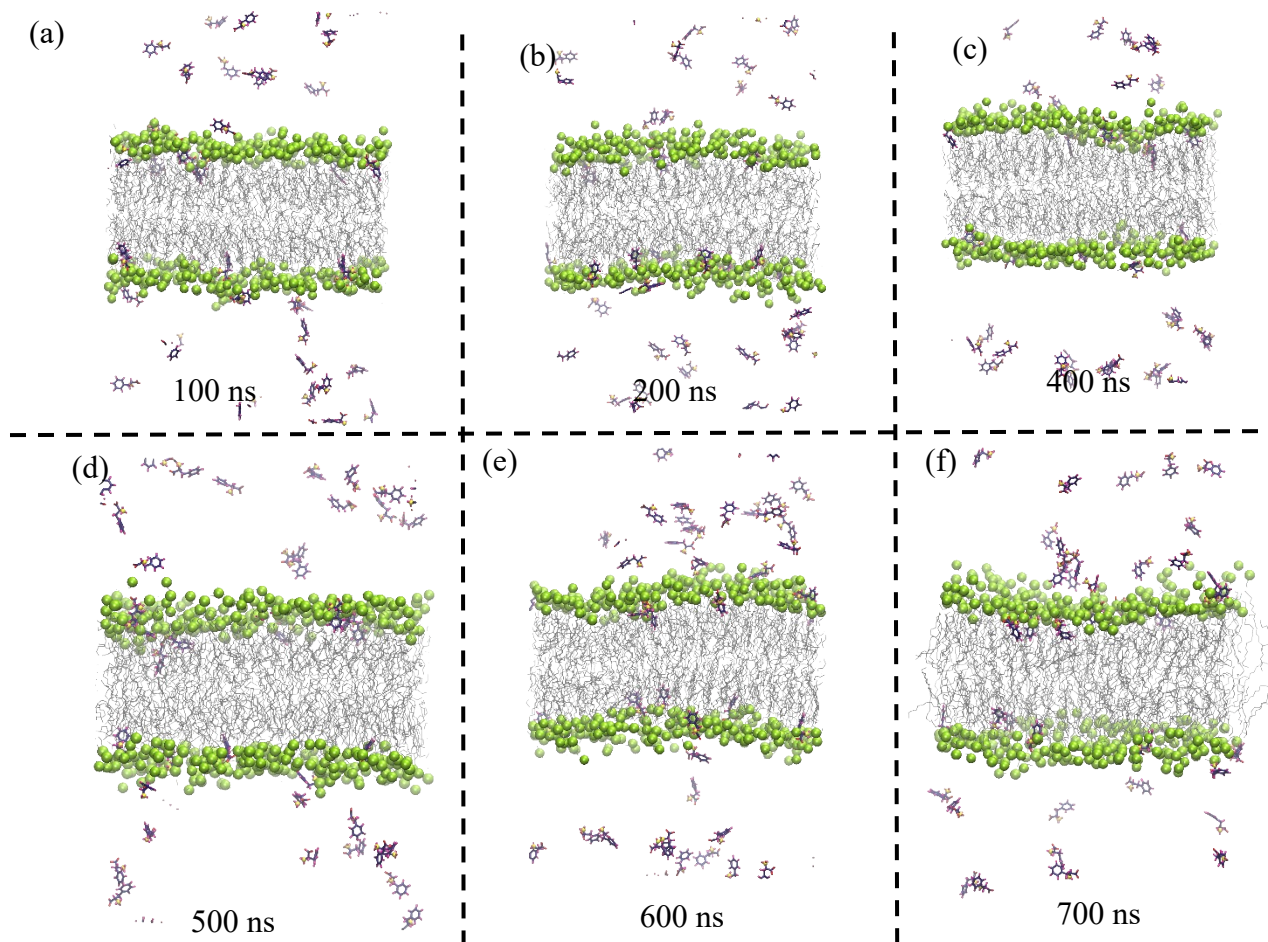

Figure S21. Snapshots of the I-Phe system showing the time-dependent structure of Phe near the DPPC lipid membrane modeled with CHARMM36 FF at 350 K. The DPPC head group atoms are shown in green VDW beads, while the acyl chains are color-coded with gray. The Phe molecules are color-coded as follows: blue (carbon), purple (nitrogen), and red (oxygen).
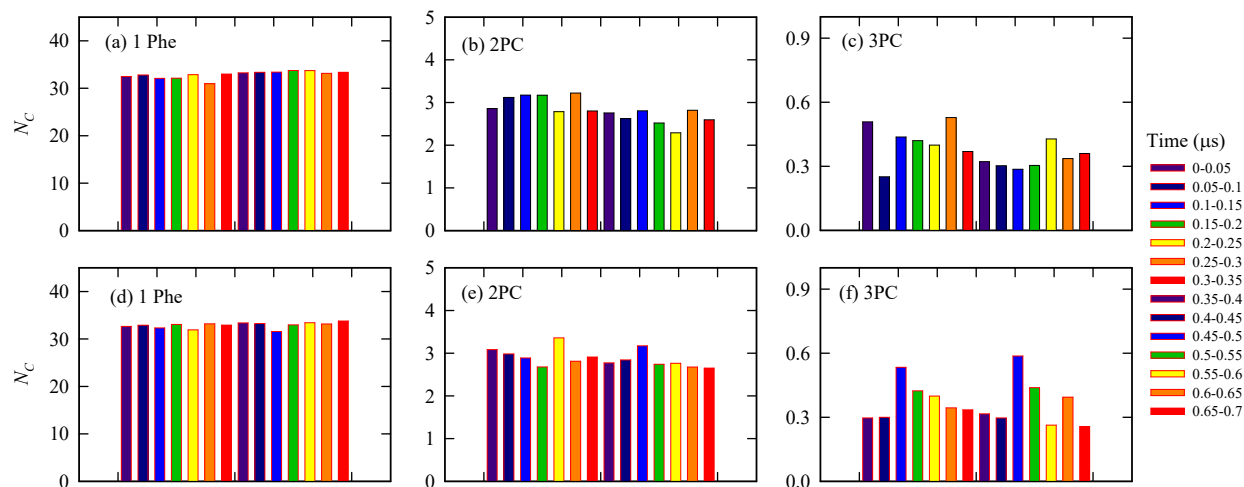
Figure S22. Time-dependent population of Phe monomer (1-Phe), dimer (2PC), and trimer (3PC) clusters of the I-Phe membrane system modeled using the CHARMM36 FF at 325 K ((a), (b), and (c)) and 350 K ((d), (e), and (f)) for the whole 700 ns simulation trajectory.

S8. Simulations of DPPC Membrane at the Physiological Temperature (310 K)

The primary objective of this work is to give explanations of the experimental observations on the effect of Phe on lipid membrane. Please note that the experiment by Vaida et al.[36], which showed that the permeability of DPPC lipid bilayer vesicle is increased by Phe, was performed at ~320 K. In addition, most of the literature experimental and simulation studies on DPPC lipid membrane are performed around 325 K.[4, 18, 39-46] The main reason for not performing the studies at room temperature or physiological temperature is that the DPPC lipid membrane exists in the gel phase at those temperatures. The fluid phase of the membrane is achieved only above 314 K, that is the experimental fluid-gel phase transition temperature T_m of DPPC lipid membrane. The simulation predicts a higher T_m value. Table S8 of ESI lists the T_m values for different FFs. All the values are higher than the experimental T_m. In the present study, the lowest temperature considered is 325 K, which is slightly higher than the temperature considered in the

experiment by Vaida et al.[36] We don't see a phase transition at 325 K. However, at 300 K or 310

K the lipid membrane should be transformed into the gel phase. To check this, we have now

simulated the membrane at 310 K with and without Phe using both OPLS/AA and CHARMM36

FFs. We observe that the lipid membrane starts freezing as shown in Figure S23. OPLS/AA

membrane shows partial freezing, while CHARMM36 membrane shows complete freezing.
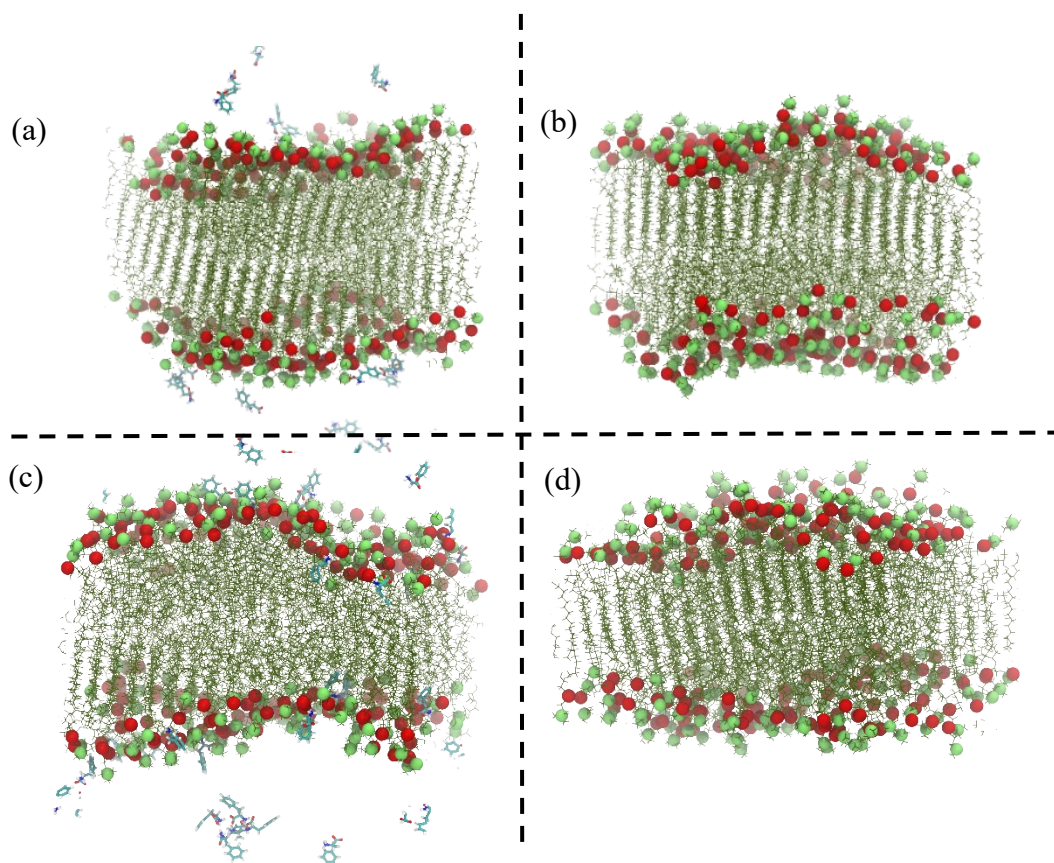
Figure S23. Snapshots showing the ordered gel phase formation in Blank DPPC membranes and I-Phe membrane systems at 310 K for ((a), (b)) CHARMM36 FF and ((c), (d)) OPLS/AA FFs, respectively. Partial freezing is observed in OPLS/AA systems.

S9. F-Phe pulling simulations

F-Phe system does not show any effect on the membrane structure and dynamics both at

325 and 350 K. The inertness mostly emanates from its weak interaction with the membrane

surface. It does not get adsorbed to the surface and thus does not induce any effect, unlike I-Phe systems. While analyzing the 700 ns long trajectory of the F-Phe system we observe that the fibril stays mostly in the bulk water region and is momentarily adsorbed. Figure S24a shows the time-dependent center of the mass distance between the fibril and the lipid bilayer. Figure S24b presents the distance distribution. The fibril prefers staying away from the membrane. The outer hydrophobic surface of the fibril structure does not favor the interactions with the hydrophilic membrane surface and imposes a large energy barrier for its penetration to the membrane core. To get a quantitative picture detailed free energy analysis is needed. This requires extensive simulations. Here, we understand the stability and adsorption of Phe fibril on the membrane surface by pulling the fibril to the membrane surface and then allow free movement. One of the terminal Phe monomers of the fibril unit is pulled to the center of mass of the phosphorus atoms on one side of the bilayer along the z-axis. We have used a harmonic force constant of 1000 kJ mol^{-1} nm^{-2} and pulled at a rate of 0.01 nm ps^{-1}. The simulation stops when the fibril is closely spaced near the membrane surface. The final configuration after the pulling is shown in Figure S25a. Next, we perform a 10 ns long restrained simulation where we restrain the z-distance between the terminal Phe of the fibril with the center of mass of the phosphorus atoms using a harmonic force constant of 1000 kJ mol^{-1} nm^{-2}. This simulation ensures equilibration of the configuration. Finally, we release the restraints and perform NPT simulation from the equilibrated configuration of the constrained simulation. As shown in Figure S25b the fibril gradually moves away from the interface and stays in the bulk. The final configuration is presented in Figure 25c at the end of the simulation. These observations corroborate our conclusion from F-Phe simulations that the Phe fibril does not adsorb to the membrane surface and prefers to stay outside in the bulk water region.
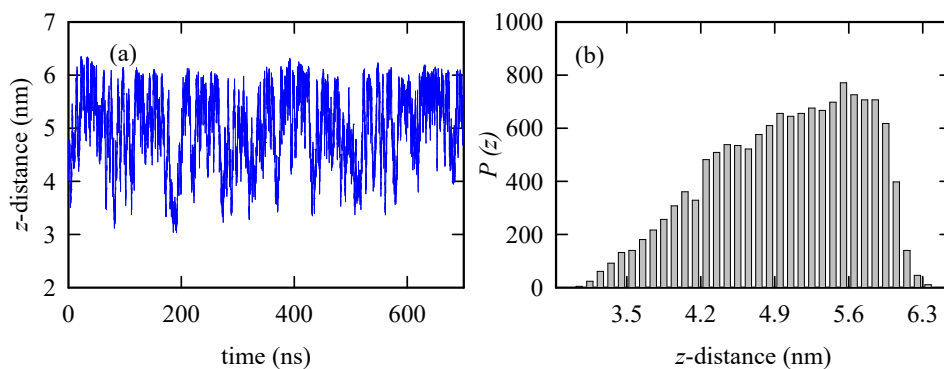
Figure S24. (a) The *z* distance between the lipid bilayer center and COM of Phe fibril in F-Phe simulations at 325 K and (b) shows the corresponding *z*-distance distribution.
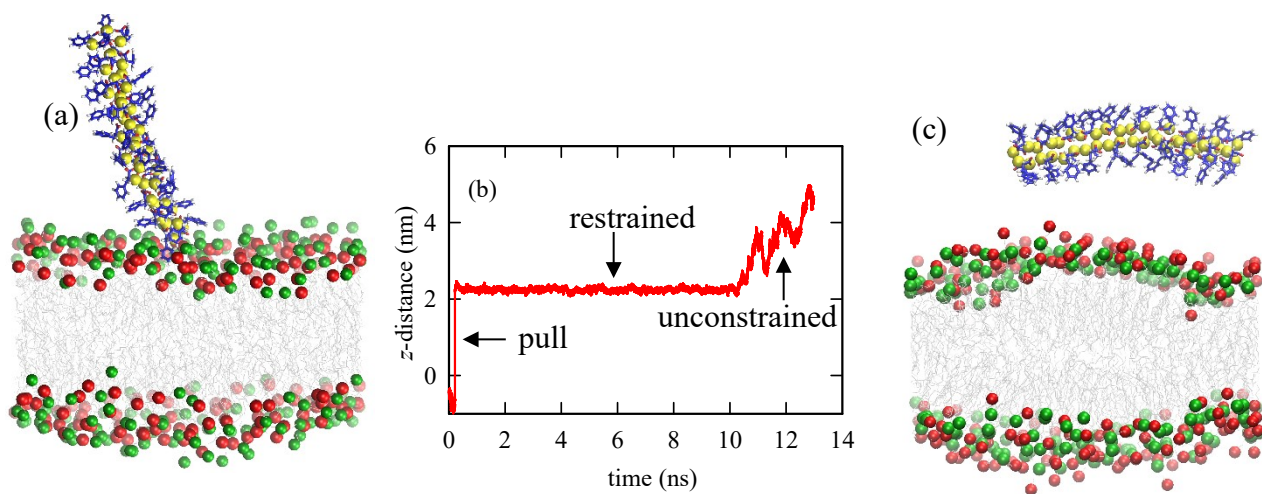
Figure S25. (a) Snapshot showing the Phe fibril pulled to the membrane surface. (b) shows the *z* distance between the lipid bilayer center and COM of Phe fibril in the three series of simulations (pulling Phe fibril, followed by 10 ns restrained simulations and finally releasing the restrain). (c) shows the position of fibril once removed with the restrain between the membrane head group atoms and Phe fibril after a ~ 3ns run. Lipid head group atoms phosphorous, nitrogen, and acyl chain are color-coded with green, red, and gray respectively. Phe fibril s color-coded with blue (carbon), yellow (nitrogen) red (oxygen), and white (hydrogen).

S10. Local Perturbation of Lipid Membrane by Different Molecules as Observed in Literature

We have proposed that two opposing forces – strong H-bonding between small Phe cluster and lipid head group and hydrophobic interaction between the phenyl group and the hydrophobic core of the lipid bilayer causes the local thinning of the lipid membrane. Similar perturbations of lipid membrane by different cell-penetrating molecules, including surfactant, protein/peptides,[47-49] Janus particles,[50] small amphiphilic molecules,[51] osmolytes,[52], etc. were observed. Preferential interactions including strong electrostatic interaction, hydrophobic interactions, and H-bonding of these molecules aligned at specific orientation in the bilayer cause membrane destabilization. Factors including the size, shape, hydrophobic profile and concentration play a crucial role in determining the extent of perturbation.

Past studies suggested the effect of amphiphilic peptides on the thickness of the lipid membrane.[47] The extent of this structural deformation depends on the orientation of peptide molecules in the bilayer. Similar disruption of lipid membrane by amyloid β (Aβ) peptides in Alzheimer's disease was revealed by Lemkul et al.[48] from a simulation based study. The intercalation of peptides to membrane induces local thinning of the lipid membrane. The strong hydrogen bonding and electrostatic interactions between the zwitterionic phospholipid head group and the peptide were seen to be the key for the membrane thinning. Local thinning of lipid membrane by α-synuclein (α–Syn) via strong electrostatic and hydrophobic interactions is observed to be the key factor of the Parkinson's disease.[49, 53, 54]

Similar alterations of membrane properties in presence of smaller amphiphilic units are also reported previously. A recent simulation study by Kumari et al.[51] shows the destabilization of PSM bilayer in the presence of ethanol molecules. Extensive hydrogen bonding interactions between ethanol molecules and the phosphate and carbonyl groups of the lipid head groups allow their intercalation into the membrane. Further, the intercalated ethanol molecules interact with

the inner hydrophobic core of the membrane via non-polar interactions. All these induce an overall destabilization of the membrane structure. A similar effect of urea on lipid membrane was also observed by Pham et al.[52]

Thinning of lipid membrane by amphiphilic nanoparticles (NPs) and ionic/non-ionic surfactant molecules are also associated with electrostatic and hydrophobic interactions with lipid molecules. A recent investigation on the effect of +/pho JNPs (cationic/hydrophobic Janus nanoparticles) by Lee et al.[50] observed such behavior with cationic and anionic lipid bilayers. Hydrophobic mismatch in the vicinity of surfactant molecules induces pronounced morphological changes in the cell membrane. Room-temperature ionic liquids (RTIL) instigate membrane swelling, observed by Jing et al.[55] narrates that the corresponding morphological changes on the lipid vesicles arise from the prominent hydrophobic interactions with the inner hydrophobic core of vesicles. The intercalated moieties induce an overall membrane thinning with the presence of tilted lipid molecules in the immediate neighborhood of the RTIL molecules. Also, the interaction of non-ionic surfactant molecules of C$_n$NO (*N*-alkyl-*N*, *N* dimethylamine *N*-oxides) homologs with PC-based bilayers is studied by small-angle X-ray diffraction by Karlovská et al.[56]. The study revealed a reduction in the membrane thickness emanating from the hydrophobic mismatch after the penetration of the surfactant molecules to EYPC bilayers. This also causes a huge local chain disordering.

S11. Comparison of the New Picture, Emerging from the Present Study, with the Earlier Literature

Some previous experimental studies made efforts to understand the detrimental effect of phenylalanine on lipid membrane to address the broader question of Phe-induced toxicity. First,

we will list the key findings of the above studies. Finally, we will discuss our new observations and show the originality of the current proposal in reference to the previous understanding.

(i) Experiment by Vaida et al.[36]

In this pioneering study, the authors measured the membrane permeability of DPPC lipid bilayer vesicles and reported the effect of Phe concentration. The authors observed that the permeability across the DPPC lipid membrane is significantly increased by increasing Phe concentration. The cryo-TEM images of the lipid vesicles did not show visible changes in size and shape of the vesicles in presence of Phe. The authors confirmed the absence of large Phe aggregates. So, how does Phe increase the membrane permeability? The above study could not show the mechanism explicitly. The authors only hypothesized that the change in permeability is probably due to either a large-scale change in the morphology of the membrane and/or a small-scale change immediately around a Phe cluster or aggregate. But these claims were not based on direct experimental facts. Therefore, the question remained unanswered: How large are the clusters and how do they exactly interact with the lipid membrane to increase the permeation? Meanwhile, the above study was consistent with the prior observation, by Vaida et al.[57] regarding the effect of L-phenylalanine on DPPC monolayer at the air-water interface. These studies showed that L-phenylalanine intercalates into a DPPC film at the air-water interface, thereby affecting the surface tension, phase morphology, and ordering of the DPPC film. However, the applicability of the results for DPPC film at the air-water interface in DPPC bilayer membrane is questionable.

Summarily, the above study showed the increase of permeability in presence of Phe without the intervention of large Phe clusters but could not address the actual mechanism. The

major question on the mechanism of increasing membrane permeability by Phe remained unanswered.

(ii) Experiments by Sarkar et al.[37, 38]

In these papers, the authors identified a polymorphic behavior of L-Phe self-assemblies in an aqueous solution. The high-resolution transmission electron microscope (HRTEM) images showed that the Phe molecules instantaneously form amyloid-like structures in water. Careful inspection revealed the presence of two distinct morphologies: net-like and rod-like. While the net-like morphologies are amorphous, the rod-like morphologies are crystalline. The transformation from the net-like to rod-like fibrils was observed on waiting for a longer time or increasing the temperature. The authors also investigated the effect of Phe on a model phospholipid membrane L-α-phosphatidylcholine (LAPC) lipid membrane. Instantaneous reduction of fluorescence intensity and broadening of fluorescence lifetime of the hydrophobic fluorescent probe is observed in presence of Phe. The diffusion of the probe also increases with the addition of Phe. All these results suggest that the packing and fluidity of the lipid membrane are affected by Phe. Since the effect is more severe in presence of instant polymorph the authors suggested that the instant polymorph, which is net-like amorphous, somehow impacts the membrane. Therefore, the above study added more information to the prior understanding. However, the key question about the mechanism of how Phe affects the membrane is unresolved.

Summarily, both the studies showed the effect of Phe on lipid membrane only indirectly. A detailed mechanism for the deleterious effect of Phe on lipid membrane was lacking. Several questions remained largely unanswered. Some of them are listed below. (i) How exactly does Phe affect the lipid membrane properties? (ii) Does the fibrillar structure have any role in

changing the membrane properties? (iii) How does the intercalation of Phe occur into the lipid membrane? (iv) Does the intercalated Phe form self-assembled structures which can modify the membrane properties? (v) How much detrimental the small Phe clusters are to the lipid membrane? Many of the questions are hard to answer using experimental techniques. We have made an effort to answer some of these questions using all-atom (AA) molecular dynamics simulation, which provides an atomistic resolution of the problem. We have shown here that very small Phe clusters (tetramer and pentamer), which would not be visible in the experimental resolution[36] can affect the lipid membrane as observed in the experiments. These clusters perturb the lipid membrane by locally thinning it. The two opposing forces, one due to the H-bonding between Phe and lipid head group and the other due to the hydrophobic interaction between phenyl group and lipid tails, induces the membrane thinning. This local thinning brings overall changes to the membrane, observed experimentally. In addition, our study suggests that the larger self-assembled oligomeric structures, which are similar to the fibrillar structures, have unfavorable interaction with the lipid membrane and thus are repelled from the membrane surface. This is opposite to the notion that the fibrillar structure affects the lipid membrane. Therefore, our study puts forward a new atomistic mechanism explaining Phe-induced perturbation of lipid bilayer.

References

1. Å. A. Skjevik, B. D. Madej, R. C. Walker and K. Teigen, *J. Phys. Chem.*, 2012, **116**, 11124-11136.
2. D. Poger and A. E. Mark, *J. Chem. Theory Comput.*, 2010, **6**, 325-336.
3. R. M. Venable, F. L. Brown and R. W. Pastor, *Chem. Phys. Lipids*, 2015, **192**, 60-74.
4. S. Erimban and S. Daschakraborty, *J. Chem. Phys.*, 2019, **151**, 065104.
5. P. Niemelä, M. T. Hyvönen and I. Vattulainen, *Biophys. J.*, 2004, **87**, 2976-2989.
6. R. M. Venable, A. Krämer and R. W. Pastor, *Chem. Rev.*, 2019, **119**, 5954-5997.

7.   S. J. Marrink and H. J. Berendsen, *J. Phys. Chem.*, 1996, **100**, 16729-16738.

8.   D. P. Tieleman, S.-J. Marrink and H. J. Berendsen, *Biochim Biophys Acta Biomembr*, 1997, **1331**, 235-270.

9.   A. Ghysels, A. Krämer, R. M. Venable, W. E. Teague, E. Lyman, K. Gawrisch and R. W. Pastor, *Nat. Commun.*, 2019, **10**, 1-12.

10.   A. Krämer, A. Ghysels, E. Wang, R. M. Venable, J. B. Klauda, B. R. Brooks and R. W. Pastor, *J. Chem. Phys.*, 2020, **153**, 124107.

11.   V. Gapsys, B. L. de Groot and R. Briones, *J. Comput. Aided Mol. Des.*, 2013, **27**, 845-858.

12.   A. Maciejewski, M. Pasenkiewicz-Gierula, O. Cramariuc, I. Vattulainen and T. Rog, *J. Phys. Chem.*, 2014, **118**, 4571-4581.

13.   W. Kulig, M. Pasenkiewicz-Gierula and T. Róg, *Chem. Phys. Lipids*, 2016, **195**, 12-20.

14.   W. Kulig, M. Pasenkiewicz-Gierula and T. Róg, *Data in Brief*, 2015, **5**, 333-336.

15.   A. Maiti and S. Daschakraborty, *J. Phys. Chem.*, 2021, **125**, 1167-1180.

16.   D. Poger and A. E. Mark, *J. Chem. Theory Comput.*, 2012, **8**, 4807-4817.

17.   K. Pluhackova, S. A. Kirsch, J. Han, L. Sun, Z. Jiang, T. Unruh and R. A. Böckmann, *J. Phys. Chem.*, 2016, **120**, 3888-3903.

18.   C. J. Dickson, B. D. Madej, Å. A. Skjevik, R. M. Betz, K. Teigen, I. R. Gould and R. C. Walker, *J. Chem. Theory Comput.*, 2014, **10**, 865-879.

19.   G. Büldt, H. Gally, J. Seelig and G. Zaccai, *J. Mol. Biol.*, 1979, **134**, 673-691.

20.   R. L. Thurmond, S. W. Dodd and M. F. Brown, *Biophys. J.*, 1991, **59**, 108-113.

21.   J. F. Nagle and S. Tristram-Nagle, *Biochim Biophys Acta Biomembr*, 2000, **1469**, 159-195.

22.   L. Lis, d. McAlister, N. Fuller, R. Rand and V. Parsegian, *Biophys. J.*, 1982, **37**, 657.

23.   A. Filippov, G. Orädd and G. Lindblom, *Biophys. J.*, 2003, **84**, 3079-3086.

24.   J. R. Silvius, *Lipid-protein interactions*, 1982, **2**, 239-281.

25.   H. I. Petrache, S. W. Dodd and M. F. Brown, *Biophys. J.*, 2000, **79**, 3172-3192.

26.   L. Sun and R. A. Böckmann, *Eur. Biophys. J.*, 2018, **47**, 151-164.

27.   P. S. Coppock and J. T. Kindt, *J. Phys. Chem.*, 2010, **114**, 11468-11473.

28.   C. T. Andrews and A. H. Elcock, *J. Chem. Theory Comput.*, 2013, **9**, 4585-4602.

29. J. Lee, X. Cheng, J. M. Swails, M. S. Yeom, P. K. Eastman, J. A. Lemkul, S. Wei, J. Buckner, J. C. Jeong, Y. Qi, S. Jo, V. S. Pande, D. A. Case, C. L. Brooks, A. D. MacKerell, J. B. Klauda and W. Im, *J. Chem. Theory Comput.*, 2016, **12**, 405-413.

30. L. Adler-Abramovich, L. Vaks, O. Carny, D. Trudler, A. Magno, A. Caflisch, D. Frenkel and E. Gazit, *Nature chemical biology*, 2012, **8**, 701-706.

31. T. D. Do, W. M. Kincannon and M. T. Bowers, *J. Am. Chem. Soc.*, 2015, **137**, 10080-10083.

32. H. W. German, S. Uyaver and U. H. Hansmann, *J. Phys. Chem. A*, 2014, **119**, 1609-1615.

33. S. Uyaver, H. W. Hernandez and M. G. Habiboglu, *Phys. Chem. Chem. Phys.*, 2018, **20**, 30525-30536.

34. M. Parrinello and A. Rahman, *J. Appl. Phys.*, 1981, **52**, 7182-7190.

35. B. Hess, H. Bekker, H. J. Berendsen and J. G. Fraaije, *J. Comput. Chem.*, 1997, **18**, 1463-1472.

36. R. Perkins and V. Vaida, *J. Am. Chem. Soc.*, 2017, **139**, 14388-14391.

37. P. Banerjee, K. Rajak, P. K. Nandi, S. Pal, M. Ghosh, S. Mishra and N. Sarkar, *J. Phys. Chem. Lett.*, 2020, **11**, 8585-8591.

38. S. Nandi, A. Pyne, M. Ghosh, P. Banerjee, B. Ghosh and N. Sarkar, *Langmuir*, 2020, **36**, 2459-2473.

39. F. Sajadi and C. N. Rowley, *PeerJ*, 2018, **6**, e5472.

40. O. Berger, O. Edholm and F. Jähnig, *Biophys. J.*, 1997, **72**, 2002-2013.

41. D. Poger, B. Caron and A. E. Mark, *Biochimica et Biophysica Acta (BBA) - Biomembranes*, 2016, **1858**, 1556-1565.

42. J. Sonne, M. Ø. Jensen, F. Y. Hansen, L. Hemmingsen and G. H. Peters, *Biophys. J.*, 2007, **92**, 4157-4167.

43. A. Kukol, *J. Chem. Theory Comput.*, 2009, **5**, 615-626.

44. D. Poger, W. F. Van Gunsteren and A. E. Mark, *J. Comput. Chem.*, 2010, **31**, 1117-1125.

45. C. J. Dickson, L. Rosso, R. M. Betz, R. C. Walker and I. R. Gould, *Soft Matter*, 2012, **8**, 9617-9627.

46. J. P. Jämbeck and A. P. Lyubartsev, *J. Phys. Chem.*, 2012, **116**, 3164-3179.

47. S. L. Grage, S. Afonin, S. Kara, G. Buth and A. S. Ulrich, *Frontiers in cell and developmental biology*, 2016, **4**, 65.

48. J. A. Lemkul and D. R. Bevan, *The FEBS journal*, 2009, **276**, 3060-3075.

49. N. P. Reynolds, A. Soragni, M. Rabe, D. Verdes, E. Liverani, S. Handschin, R. Riek and S. Seeger, *J. Am. Chem. Soc.*, 2011, **133**, 19366-19375.

50. K. Lee and Y. Yu, *Soft Matter*, 2019, **15**, 2373-2380.

51. P. Kumari, S. Kaur, S. Sharma and H. K. Kashyap, *J. Chem. Phys.*, 2018, **148**, 165102.

52. Q. D. Pham, A. Wolde-Kidan, A. Gupta, A. Schlaich, E. Schneck, R. R. Netz and E. Sparr, *J. Phys. Chem.*, 2018, **122**, 6471-6482.

53. J. Parres-Gold, A. Chieng, S. Wong Su and Y. Wang, *ACS Chemical Neuroscience*, 2020, **11**, 2528-2534.

54. M. Manna and R. K. Murarka, *ACS Chemical Neuroscience*, 2021, **12**, 675-688.

55. B. Jing, N. Lan, J. Qiu and Y. Zhu, *J. Phys. Chem.*, 2016, **120**, 2781-2789.

56. J. Karlovská, K. Lohner, G. Degovics, I. Lacko, F. Devínsky and P. Balgavý, *Chem. Phys. Lipids*, 2004, **129**, 31-41.

57. E. C. Griffith, R. J. Perkins, D.-M. Telesford, E. M. Adams, L. Cwiklik, H. C. Allen, M. Roeselová and V. Vaida, *J. Phys. Chem.*, 2015, **119**, 9038-9048.